

The evolution of the UV-to-mm extragalactic background light: evidence for a top-heavy initial mass function?

William I. Cowley,¹ Cedric G. Lacey¹,² Carlton M. Baugh,^{2*} Shaun Cole,²
Carlos S. Frenk² and Claudia del P. Lagos^{3,4,5}

¹*Kapteyn Astronomical Institute, University of Groningen, PO Box 800, NL-9700 AV Groningen, the Netherlands*

²*Institute for Computational Cosmology, Department of Physics, University of Durham, South Road, Durham DH1 3LE, UK*

³*International Centre for Radio Astronomy Research (ICRAR), M468, University of Western Australia, 35 Stirling Hwy, Crawley, WA 6009, Australia*

⁴*Australian Research Council Centre of Excellence for All-sky Astrophysics (ASTRO 3D)*

⁵*Cosmic Dawn Center (DAWN), Niels Bohr Institute, University of Copenhagen, Juliane Maries vej 30, DK-2100 Copenhagen, Denmark*

Accepted 2019 May 14. Received 2019 May 14; in original form 2018 August 15

ABSTRACT

We present predictions for the UV-to-mm extragalactic background light (EBL) from a recent version of the GALFORM semi-analytical model of galaxy formation which invokes a top-heavy stellar initial mass function (IMF) for galaxies undergoing dynamically triggered bursts of star formation. We combine GALFORM with the GRASIL radiative transfer code for computing fully self-consistent UV-to-mm spectral energy distributions for each simulated galaxy, accounting for the absorption and re-emission of stellar radiation by interstellar dust. The predicted EBL is in near-perfect agreement with recent observations over the whole UV-to-mm spectrum, as is the evolution of the cosmic spectral energy distribution over the redshift range for which observations are available ($z \lesssim 1$). We show that approximately 90 per cent of the EBL is produced at $z < 2$ although this shifts to higher redshifts for sub-mm wavelengths. We assess whether the top-heavy IMF in starbursts is necessary in order to reproduce the EBL at the same time as other key observables, and find that variant models with a universal solar-neighbourhood IMF display poorer agreement with EBL observations over the whole UV-to-mm spectrum and fail to match the counts of galaxies in the sub-mm.

Key words: galaxies: evolution – galaxies: formation – infrared: galaxies – submillimetre: galaxies – ultraviolet: galaxies.

1 INTRODUCTION

The extragalactic background light (EBL) provides a record of the production of photons since (re)combination, and thus contains a wealth of information regarding various astrophysical processes over the history of the Universe. In the 0.1–1000 μm (UV-to-mm) wavelength range it is dominated by the redshifted emission from galaxies, including the absorption and re-emission by interstellar dust of photons produced in stars. It also includes minor ($\lesssim 10$ per cent) contributions from active galactic nuclei (e.g. Almaini, Lawrence & Boyle 1999; Silva, Maiolino & Granato 2004), intra-halo light (IHL) from diffuse halo stars no longer associated with a host galaxy (e.g. Zemcov et al. 2014) and redshifted Lyman α emission from the epoch of reionization (e.g. Mitchell-Wynne et al. 2015). As such, the EBL provides strong constraints on the cosmic star formation history and on models of galaxy formation and evolution (e.g. Fardal et al. 2007; Franceschini, Rodighiero &

Vaccari 2008; Finke, Razzaque & Dermer 2010; Somerville et al. 2012; Inoue et al. 2013; Andrews et al. 2018; Baes et al. 2019).

Historically, two methods have been used to observationally estimate the EBL: (i) direct detection with instruments such as the diffuse infrared background explorer (Silverberg et al. 1993) and the far-infrared absolute spectrophotometer (Mather, Fixsen & Shafer 1993) flown on the Cosmic Background Explorer satellite (*COBE*; e.g. Puget et al. 1996; Fixsen et al. 1998; Wright 2004); and (ii) integrating galaxy number counts (e.g. Madau & Pozzetti 2000; Berta et al. 2011; Béthermin et al. 2012; Driver et al. 2016). The former requires accurate removal of foregrounds, most notably that of zodiacal light (solar emission scattered by interplanetary dust e.g. Bernstein, Freedman & Madore 2002; Mattila 2006) and emission from the Milky Way (e.g. Bernard et al. 1994; Arendt et al. 1998), which have put a limit on the accuracy with which the EBL can be measured directly. The second method requires an extrapolation to faint fluxes as is discussed in more detail below.

Integrating galaxy number counts has, until relatively recently, suffered from insufficiently deep data, particularly at far-IR wavelengths, to fully resolve the EBL. In this wavelength regime

* E-mail: c.m.baugh@durham.ac.uk

confusion noise introduced by the coarse angular resolution [~ 20 arcsec full width at half maximum] of single-dish telescopes commonly used for imaging at these wavelengths and the high surface density of detectable objects (e.g. Nguyen et al. 2010) meant that only a small fraction (~ 15 per cent) of the far-IR EBL could be resolved (Oliver et al. 2010). The use of techniques such as gravitational lensing (e.g. Smail, Ivison & Blain 1997; Knudsen, van der Werf & Kneib 2008; Chen et al. 2013), stacking (e.g. Béthermin et al. 2012; Geach et al. 2013), and high-resolution interferometry (e.g. Hatsukade et al. 2013; Carniani et al. 2015) has allowed galaxy number counts to be statistically estimated at fluxes fainter than the traditional confusion limit. This has resolved a much higher proportion of the EBL, and results from direct detection and from integrated number counts are now in good agreement over mid- to far-IR wavelengths. There exists a general discrepancy between integrated counts and direct measurements at optical/near-IR wavelengths however, with direct observational estimates typically being factors of ~ 2 – 5 higher than those obtained from the integrated counts. This could indicate that sources of light not associated with individual galaxies (e.g. IHL) form a significant component of the EBL at these wavelengths, or that the models used in foreground removal require revision.

Recently, a third, independent, method of estimating the EBL has shed some light on this issue. Measurements of the attenuation of high-energy (TeV) photons from blazars, which are assumed to be emitted with a well-defined power-law spectrum, as they scatter with EBL photons could reveal the spectrum of the EBL. This was first illustrated by the High Energy Stereoscopic System (Aharonian et al. 2006), and detailed measurements have since been performed over the full UV-to-mm range (Biteau & Williams 2015; Ahnen et al. 2016). These independent measurements all favour the estimates from integrated number counts (though some caveats do remain e.g. their dependence on the assumed intrinsic shape of the blazar spectrum), suggesting that current zodiacal light models may require some revision, and that light not associated with galaxies e.g. IHL, makes a minimal contribution (see also the discussion in Driver et al. 2016). For this reason, throughout we take the observed EBL as being equivalent to what is obtained from integrating galaxy number counts at all UV-to-mm wavelengths.

Here we present predictions for the EBL from the well-established semi-analytical model for galaxy formation, GALFORM (e.g. Cole et al. 2000; Lacey et al. 2016). This provides a physical calculation of galaxy formation from high redshift ($z \gtrsim 15$) to the present day ($z = 0$), accounting for the main physical processes involved (e.g. gravitational collapse, gas cooling, star formation, and feedback) implemented within the cold dark matter (CDM) cosmological model. Simulated galaxy spectral energy distributions (SEDs) are computed using the radiative transfer code GRASIL (Silva et al. 1998). This means the absorption, scattering, and re-emission of stellar radiation by interstellar dust are calculated completely self-consistently from the physical properties of galaxies predicted by GALFORM (e.g. gas-phase metallicity, size) and the assumed geometry and composition of the interstellar dust. The model thus provides a consistent physical framework for interpreting multiwavelength observations over the history of the Universe.

This combined modelling represents a significant advantage over empirical models that employ arbitrary phenomenological recipes to reproduce key observational constraints (and thus forgo a physical interpretation of their predictions e.g. Franceschini et al. 2008; Domínguez et al. 2011; Andrews et al. 2018), and over models that rely on empirical SED templates for calculating galaxy spectra over some (e.g. far-IR) or all of the UV-to-mm spectrum (as their

predicted luminosities are not necessarily internally self-consistent with the underlying galaxy formation model e.g. Gilmore et al. 2012; Somerville et al. 2012). Additionally, the flexibility of the semi-analytical method means that variant models in which some modelling assumptions are varied can be calculated quickly to assess their impact on reproducing various observations. This type of parameter exploration is not generally possible with the current state-of-the-art hydrodynamical cosmological galaxy formation simulations (e.g. Vogelsberger et al. 2014; Schaye et al. 2015; Nelson et al. 2018) due to their prohibitive computational expense.

One of the key features of the version of the GALFORM model used in this work (and described fully in Lacey et al. 2016) is that it incorporates a top-heavy initial mass function (IMF) during periods of dynamically triggered star formation. This feature was incorporated into the model so that it could simultaneously reproduce the number counts and redshift distribution of sub-mm galaxies observed at $850 \mu\text{m}$ and the present-day (i.e. $z = 0$) optical and near-IR galaxy luminosity functions (Baugh et al. 2005). The IMF used in the Lacey et al. (2016) model is much less top-heavy, however, than the one implemented by Baugh et al. We investigate whether this feature is required in order for the model to reproduce the EBL at far-IR wavelengths in conjunction with other constraints such as the K -band luminosity function at $z = 0$ and the evolution of the cosmic star formation rate density. In doing so we reassess the argument of Fardal et al. (2007), who suggest that these three observational datasets are incompatible with a universal IMF of the form observed in the solar neighbourhood. Fardal et al. integrated simple parametrizations of the cosmic star formation history and found that it was not possible to find histories that could reproduce the local K -band luminosity density and the EBL simultaneously whilst assuming a Salpeter (1955) IMF (see e.g. their fig. 5). We note that Somerville et al. (2012), using a semi-analytical galaxy formation model assuming a universal IMF, found a reasonable match to the EBL, cosmic star formation history and present-day K -band luminosity function, but underpredicted the number counts of galaxies at $850 \mu\text{m}$. Other galaxy formation studies have considered IMF variations, such as Gargiulo et al. (2015) and Fontanot et al. (2017), who invoked a top-heavy IMF in regions of high star formation in semi-analytical models, and Barber, Crain & Schaye (2018), who imposed a pressure-dependent IMF in an EAGLE hydrodynamical simulation; these studies did not consider the EBL.

This paper is structured as follows: in Section 2 we introduce the theoretical model, which incorporates a semi-analytical model of galaxy formation implemented within halo merger trees derived from a Millennium-style dark matter only N -body simulation (Springel et al. 2005; Baugh et al. 2019) and the radiative transfer code, GRASIL (Silva et al. 1998), for computing the absorption and re-emission of stellar radiation by interstellar dust. In Section 3 we present the predictions of the model for the EBL and show how this is built up over the history of the Universe.¹ We also present predictions from variant models with a universal solar-neighbourhood IMF and discuss how critical this feature is for reproducing the EBL. We summarize in Section 4. Throughout we assume a flat Λ CDM cosmology with cosmological parameters consistent with recent *Planck* satellite results (Planck Collaboration XVI 2014).²

¹Some of the model data presented here will be made available at <http://icc.dur.ac.uk/data/>. For other requests please contact the first author.

² $\Omega_m = 0.307$, $\Omega_\Lambda = 0.693$, $h = 0.678$, $\Omega_b = 0.0483$, $\sigma_8 = 0.829$

2 THE MODEL

Here we introduce our theoretical model, which combines a dark matter only N -body simulation, a semi-analytical model of galaxy formation (GALFORM) and the spectrophotometric radiative transfer code GRASIL (Silva et al. 1998) for computing self-consistent UV-to-mm galaxy SEDs.

2.1 The *Planck* Millennium dark matter simulation

Galaxies are assumed to form from baryonic condensation within the potential wells of dark matter haloes, with their subsequent evolution being controlled in part by the merging history of the halo (White & Rees 1978). Here halo merger trees are extracted directly from a dark matter only N -body simulation (e.g. Helly et al. 2003; Jiang et al. 2014). We use a new (800 Mpc)³ Millennium-style simulation (Springel et al. 2005) with cosmological parameters consistent with recent *Planck* satellite results (Planck Collaboration XVI 2014), henceforth referred to as the P-Millennium (Baugh et al. 2019; see also McCullagh et al. 2017; Cowley et al. 2018). The large volume, (800 Mpc)³, gives the bright end of the predicted luminosity functions greater statistical precision.

The halo mass resolution of this simulation is $2.12 \times 10^9 h^{-1} M_{\odot}$, where a halo is required to have at least 20 dark matter particles and is defined according to the ‘DHalo’ algorithm (Jiang et al. 2014). This mass resolution is approximately an order of magnitude better than previous dark matter simulations that were used with this galaxy formation model. For example, the MR7 simulation (Springel et al. 2005; Guo et al. 2013) in which the Lacey et al. (2016) model was originally implemented has a halo mass resolution of $1.87 \times 10^{10} h^{-1} M_{\odot}$. Not only does this mean that the model is able to make predictions for smaller mass haloes (i.e. fainter galaxies) but also that the more moderate mass haloes ($\sim 10^{11} - 10^{12} h^{-1} M_{\odot}$) that in this model dominate the far-IR background (Cowley et al. 2016) are resolved with greater precision. The P-Millennium merger trees also provide a finer temporal resolution than MR7 but this does not have any significant impact on this model.

2.2 Semi-analytical galaxy formation

Baryonic physics in GALFORM are included as a set of coupled differential equations that track the exchange of mass and metals between the stellar, cold disc gas and hot halo gas components in a given halo. These equations include simplified prescriptions for the physical processes (e.g. gas cooling, star formation, and feedback) known to be important for galaxy formation. We discuss some of the main features of the model below and refer the interested reader to Lacey et al. (2016) for more details.

There are, however, minor changes to the values of two parameters from the model presented by Lacey et al. These are described in more detail in Baugh et al. (2019), see also section 2.1.5 and table 1 of Cowley et al. (2018), and mainly account for the fact that the underlying halo merger trees within which the model is implemented are generated from a dark matter simulation with improved halo mass resolution (see above) and different cosmological parameters, so that the model can reproduce the original calibration data to a similar level of fidelity. The impact that this recalibration has on the predicted EBL is discussed in Appendix D.

2.2.1 Star formation and stellar initial mass function

Cold disc gas is partitioned into molecular and atomic components according to the mid-plane gas pressure in the disc. The star

formation rate surface density is then assumed to be proportional to the surface density of molecular gas, such that

$$\Sigma_{\text{SFR}} = \nu_{\text{SF}} \Sigma_{\text{mol}} = \nu_{\text{SF}} f_{\text{mol}} \Sigma_{\text{cold}}, \quad (1)$$

where $f_{\text{mol}} = R_{\text{mol}}/(1 + R_{\text{mol}})$, R_{mol} is the local ratio of molecular and atomic gas surface densities, i.e. $R_{\text{mol}} = \Sigma_{\text{mol}}/\Sigma_{\text{atom}}$ and the parameter $\nu_{\text{SF}} = 0.74 \text{ Gyr}^{-1}$, based on the observations of Bigiel et al. (2011). This expression is then integrated over the whole disc to yield the global star formation rate, ψ . For further details of this star formation law, see Lagos et al. (2011). For star formation in the galactic disc a Kennicutt (1983) IMF is assumed. This IMF is described by $x = 0.4$ in $dN/d\ln m \propto m^{-x}$ for $m < 1 M_{\odot}$ and $x = 1.5$ for $m > 1 M_{\odot}$ [for reference, a Salpeter (1955) IMF has an unbroken slope of $x = 1.35$].

Galaxy starbursts are triggered by dynamical processes. These are either a bar instability in the disc applying the stability criterion of (Efstathiou, Lake & Negroponte 1982, see Section 3.6.2 of Lacey et al. for further details) or major galaxy mergers (and some gas-rich minor mergers). Throughout this work ‘(star)bursts’ refer to such dynamically triggered star formation event rather than, for example, to a galaxy’s position on the specific star formation rate–stellar mass plane. This distinction is discussed in Cowley et al. (2017). Burst star formation takes place in a forming galactic bulge. It is assumed that $f_{\text{mol}} \approx 1$ in bursts and that the star formation rate depends on the dynamical time-scale of the bulge as

$$\psi_{\text{burst}} = \nu_{\text{SF,burst}} M_{\text{cold,burst}}, \quad (2)$$

where $\nu_{\text{SF,burst}} = 1/\tau_{\star,\text{burst}}$ and

$$\tau_{\star,\text{burst}} = \max[f_{\text{dyn}} \tau_{\text{dyn,bulge}}, \tau_{\text{burst,min}}]. \quad (3)$$

Here $\tau_{\text{dyn,bulge}}$ is the dynamical time-scale of the bulge and f_{dyn} and $\tau_{\text{burst,min}}$ are model parameters. This means that for large dynamical times the star formation rate scales mostly with the dynamical time, but has a ceiling value when the dynamical time of the bulge is short. Here $f_{\text{dyn}} = 20$ and $\tau_{\text{burst,min}} = 100 \text{ Myr}$ (Lacey et al. 2016).

For star formation in bursts, it is assumed that stars form with a top-heavy IMF, described by a slope of $x = 1$.

This assumption is primarily motivated by the requirement that the model reproduces the observed far-IR/sub-mm galaxy number counts and redshift distributions (e.g. Baugh et al. 2005; Lacey et al. 2016). It should be noted that the IMF slope in this new model is much less top-heavy than the $x = 0$ one used by Baugh et al. (2005).

The assumption of a top-heavy IMF for starburst galaxies is often seen as controversial. For example, in their review of observational studies Bastian, Covey & Meyer (2010) argue against significant IMF variations in the local Universe. However, Ballero, Kroupa & Matteucci (2007) argue through chemical evolution modelling that an $x \sim 1$ slope is required to explain the [Fe/H] distribution in the bulges of the Milky Way and M31. Additionally, Gunawardhana et al. (2011) infer an IMF for nearby star-forming galaxies that becomes more top-heavy with increasing star formation rate, reaching a slope of $x \approx 0.9$; and a similar IMF slope was inferred for a star-forming galaxy at $z \sim 2.5$ by Finkelstein et al. (2011). Both of these studies use modelling of a combination of nebular emission and broadband photometry to infer the IMF slope. More recently, Romano et al. (2017) inferred an IMF slope of $x = 0.95$ in nearby starburst galaxies through modelling the observed CNO isotopic ratios. This method has since been extended to dust-obscured star-forming galaxies at $z \sim 2-3$ by Zhang et al. (2018), who claim unambiguous evidence for a similarly top-heavy IMF ($x = 0.95$) in four gravitationally lensed sub-mm galaxies. Evidence for a top-heavy IMF has also been found in local star-forming regions. A recent

study of massive stars ($m \gtrsim 15 M_{\odot}$) in the 30 Doradus region in the Large Magellanic Cloud found an IMF slope of 0.9 ± 0.3 (Schneider et al. 2018a).³ Thus, whilst the issue of a varying IMF is far from resolved, there is a growing number of observational studies that support both our assumption and adopted value of $x = 1$. We note, however, that the debate about the form of the IMF continues and a number of studies support a revision to the IMF in the opposite sense to that proposed here, in the direction of being more bottom-heavy (e.g. Smith et al. 2015; La Barbera et al. 2016; Collier, Smith & Lucey 2018).

2.2.2 Supernovae feedback

The injection of energy into the ISM from supernovae (SN) is assumed to eject gas from the disc to beyond the virial radius of the halo at a rate \dot{M}_{eject} . As SN are short-lived, this rate is proportional to the instantaneous star formation rate, ψ , according to a ‘mass loading’ factor, β , such that

$$\dot{M}_{\text{eject}} = \beta(V_c) \psi = (V_c/V_{\text{SN}})^{-\gamma_{\text{SN}}} \psi. \quad (4)$$

Here V_c is the circular velocity of the disc; ψ is the star formation rate; and V_{SN} and γ_{SN} are adjustable parameters. We assume $V_{\text{SN}} = 320 \text{ km s}^{-1}$ (Lacey et al. 2016) and $\gamma_{\text{SN}} = 3.4$ (Baugh et al. 2019). The ejected gas accumulates in a reservoir of mass, M_{res} , and then falls back within the virial radius at a rate inversely proportional to the dynamical time-scale of the halo.

2.3 Radiative transfer

We use the spectrophotometric radiative transfer code GRASIL (Silva et al. 1998) to compute model galaxy SEDs. Using the star formation and metal enrichment histories, gas masses and galaxy structural parameters predicted by GALFORM, and assuming a composition and geometry for interstellar dust, GRASIL computes the SEDs of the model galaxies, accounting for dust extinction (absorption and scattering) of stellar radiation and its subsequent re-emission. Here we briefly describe the GRASIL model (for further details see Silva et al. 1998 and Granato et al. 2000).

GRASIL assumes that stars exist in a disc+bulge system, as is the case in GALFORM. The disc has a radial and vertical exponential profile with scale lengths, h_R and h_z , and the bulge is described by an analytic King model profile, $\rho \propto (r^2 + r_c^2)^{-3/2}$ out to a truncation radius, r_t . The half-mass radii, r_{disc} and r_{bulge} , are predicted by GALFORM (see Cole et al. 2000, for more details). By definition, given the assumed profiles, the bulge core radius is related to the half-mass radius by $r_c = r_{\text{bulge}}/14.6$, whilst the radial disc scale length, h_R , is related to the disc half-mass disc radius by $h_R = r_{\text{disc}}/1.68$. Star formation histories are calculated separately for the disc and bulge by GALFORM. For galaxies undergoing a starburst, the burst star formation, as well as the associated gas and dust, are assumed also to be in an exponential disc but with a half-mass radius $r_{\text{burst}} = \eta r_{\text{bulge}}$, rather than r_{disc} , where η is an adjustable parameter (here $\eta = 1$; see Granato et al. 2000). The disc axial ratio, h_z/h_R , is a parameter of the GRASIL model; for starburst galaxies, the axial ratio of the burst is allowed to be different (0.5) from that of discs in quiescent galaxies (0.1).

³A subsequent analysis of the data used by Schneider et al. found a slightly different value, $x = 1.05^{+0.13}_{-0.14}$ (Farr & Mandel 2018), which is still top-heavy relative to that of the solar neighbourhood and with a smaller uncertainty than determined by Schneider et al. See also Schneider et al. (2018b).

The gas and dust exist in an exponential disc, with the same radial scale length as the disc stars but in general with a different scale height, so $h_z(\text{dust})/h_z(\text{stars})$ is an adjustable parameter. The gas and dust are assumed to exist in two components: (i) giant molecular clouds in which stars form, escaping on some time-scale, t_{esc} ; and (ii) a diffuse cirrus ISM. The total gas mass, M_{cold} , and gas-phase metallicity, Z_{cold} , are calculated by GALFORM. The fraction of gas in molecular clouds is determined by the parameter f_{cloud} . The cloud mass, m_{cloud} , and radius, r_{cloud} , are also parameters, though the results of the model depend only on the ratio, $m_{\text{cloud}}/r_{\text{cloud}}^2$, which determines (together with the gas metallicity) the optical depth of the clouds.

The dust is assumed to consist of a mixture of graphite and silicate grains and polycyclic aromatic hydrocarbons (PAHs), each with a distribution of grain sizes. The grain mix and size distribution were determined by Silva et al. so that the extinction and emissivity properties of the local ISM are reproduced using the optical properties of the dust grains tabulated by Draine & Lee (1984). At long wavelengths ($\lambda > 30 \mu\text{m}$) this results in a dust opacity that approximates $\kappa_d \propto \lambda^{-2}$. However, in galaxies undergoing a starburst this is modified (for $\lambda > 100 \mu\text{m}$) such that $\kappa_d \propto \lambda^{-\beta_b}$, where β_b is treated as an adjustable parameter. Laboratory measurements suggest that values in the range $\beta_b = 1.5\text{--}2$ are acceptable (Agladze et al. 1996) and more recent experiments that hotter dust favour lower values of β_b (Boudet et al. 2005). Note that in our model burst galaxies have higher dust temperatures on average than their quiescently star-forming counterparts (Cowley et al. 2017). Here a value of $\beta_b = 1.5$ is adopted (Lacey et al. 2016). The total dust mass in a galaxy is proportional to the cold gas mass and metallicity, both of which are predicted by GALFORM.

We use the stellar population synthesis models of Maraston (2005), adopting a Kennicutt (1983) IMF for stars that form quiescently and a top-heavy IMF for stars made in bursts. For calculating broadband photometry we convolve the predicted galaxy SED with the relevant filter transmission, and assume the prescription of Meiksin (2005) for attenuation due to the intergalactic medium. Note that we do not change any adjustable GRASIL parameters from the values we have used in previous works (see e.g. values in table 2 of Cowley et al. 2018).

Due to the computational expense of the radiative transfer calculation, we select a sub-sample of galaxies from GALFORM’s original output on which to run GRASIL. Similarly to Cowley et al. (2018), where the same model was used to make predictions for forthcoming deep galaxy surveys with the *James Webb Space Telescope*, we sample galaxies according to their stellar mass; however, here we also ensure that within each stellar mass bin the specific star formation rate distribution is fairly sampled.

2.4 Calculating predicted quantities

We now briefly explain how the model predictions are calculated from the output galaxy SEDs and how various quantities are related to each other. An observed frequency is denoted by ν , which is related to the emitted frequency, ν_e , by $\nu = \nu_e(1+z)$.

Once our output SEDs have been convolved with the appropriate (redshifted) filter transmission it is possible to construct the luminosity function, $dn/d\ln L_{\nu}$, at each output time. This is then related to the galaxy number counts, $d\eta/d\ln S_{\nu}$ (we use η here to denote the surface number density of galaxies, rather than n which we use for

the comoving number density), by

$$\frac{d\eta}{d \ln S_\nu} = \int \frac{dn}{d \ln L_{\nu(1+z)}} \frac{dV}{dz}, \quad (5)$$

where dV/dz is the comoving volume element per unit solid angle and flux is related to luminosity according to

$$S_\nu = (1+z) \frac{L_{\nu(1+z)}}{4\pi d_L^2(z)}, \quad (6)$$

where $d_L(z)$ is the luminosity distance to redshift z . The EBL, I_ν , the intensity per unit frequency per unit solid angle, is then simply the flux-weighted integral of the number counts

$$I_\nu = \int S_\nu \frac{d\eta}{d \ln S_\nu} d \ln S_\nu. \quad (7)$$

The EBL can also be calculated directly from the CSED, ε_ν , which describes the luminosity density per unit frequency at a given epoch, and is the luminosity-weighted integral of the luminosity function,⁴

$$\varepsilon_\nu = \int L_\nu \frac{dn}{d \ln L_\nu} d \ln L_\nu. \quad (8)$$

To obtain the EBL this is then integrated according to

$$I_\nu = \int (1+z) \frac{\varepsilon_{\nu(1+z)}}{4\pi d_L^2(z)} \frac{dV}{dz} dz. \quad (9)$$

The total EBL intensity (or brightness) per unit solid angle at $z = 0$, I , is then obtained by integrating over frequency:

$$I = \int \nu I_\nu d \ln \nu. \quad (10)$$

This is often divided into the optical/near-IR intensity, I_{COB} , and the far-IR intensity, I_{CIB} , where the integral in equation (10) is performed between $\lambda_{\text{obs}} = (0.1, 8)$ and $(8, 1000)$ μm , respectively.

2.5 Variant models with a universal IMF

We also investigate two variant GALFORM models to illustrate the effect of relaxing the assumption of a top-heavy IMF in bursts which is a key component of the fiducial model. Note that we do not consider either of these variants to be viable models as they fail to reproduce the calibration data to the same level as the fiducial model, as discussed below.

In the first variant model we turn off the top-heavy IMF option in the fiducial model such that all stars form with a universal Kennicutt (1983) IMF, but leave all other parameters unchanged (this variant is labelled lc16.kenn83). The predicted K -band luminosity function for this model is shown in Fig. 1. This variant matches the fiducial model faintwards of L_* but underpredicts the number of bright galaxies by up to a factor of two. This is because in the fiducial model only a small fraction ($\lesssim 5$ per cent) of the $z = 0$ stellar mass density was formed in dynamically triggered bursts with a top-heavy IMF (e.g. González et al. 2011).

As well as underpredicting the bright-end of the present-day luminosity function, we will see later that this model dramatically fails to reproduce the mid- to far-IR EBL, which relates also to the generally poor agreement with the cosmic star formation history (see Section 3.4 and Figs 7 and 8). To mitigate these shortcomings, we also consider another variant model in which, as well as assuming a universal IMF, we also reduce the value of

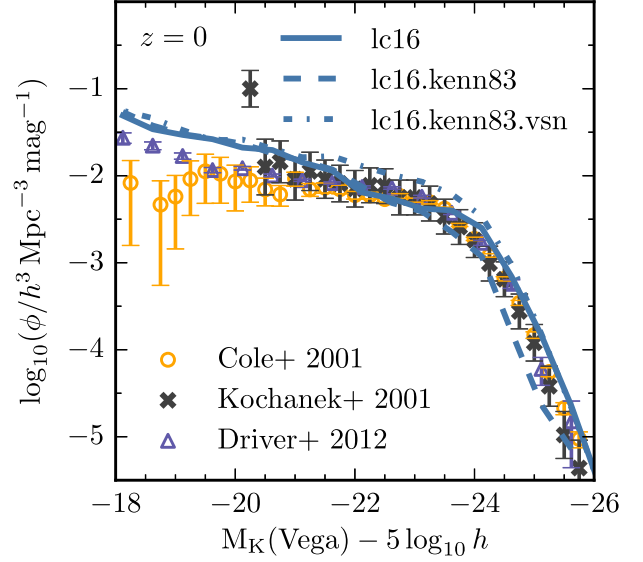


Figure 1. The K -band luminosity function at $z = 0$. Model predictions are from the fiducial model (lc16, solid line), a variant with a universal Kennicutt (1983) IMF (lc16.kenn83, dashed line) and a variant with a universal IMF and a lower supernovae feedback mass-loading normalization (lc16.kenn83.vsn, dash-dotted line). Luminosity function data are from Cole et al. (2001), Kochanek et al. (2001), and Driver et al. (2012).

the V_{SN} parameter, which controls the normalization of the mass-loading factor for supernova feedback (see equation 4), from 320 to 290 km s^{-1} , resulting in the model labelled lc16.kenn83.vsn. The predicted K -band luminosity function for this variant is also shown in Fig. 1; the match to the observed bright end is much better in this case. However, this variant model overpredicts the abundance of galaxies around L_* .

3 RESULTS

Here we present the predicted UV-to-mm EBL spectrum, and show from which redshifts it originates (Section 3.1). We also present the predicted model number counts compared to the observational estimates compiled by Driver et al. (2016), and the predicted distribution of EBL emission redshifts (Section 3.2). We compare these redshift distributions at far-IR wavelengths to those inferred from CMB cross-correlations (Schmidt et al. 2015) and stacked *Herschel* data (Jauzac et al. 2011; Béthermin et al. 2012). In Section 3.3 we present the evolution of the CSED, ε_ν , predicted by our model, compared with the observational estimates of Andrews et al. (2017). Finally, in Section 3.4, we review the consistency of the EBL, the $z = 0$ K -band luminosity function and the cosmic star formation history in the context of one of the more controversial features of our model, namely a top-heavy IMF for starburst galaxies.

3.1 The extragalactic background light

The EBL predicted by our model is shown in Fig. 2, compared to observational data derived from a variety of methods. Different observational datasets are generally in good agreement with one another, though the discrepancy at near-IR wavelengths is evident between the direct estimates of Wright (2004), based on data from the *COBE* satellite, and the other indirect methods, as discussed in the Introduction. As described there, current data favour the

⁴It can also be thought of as the volume-weighted sum of our output GRASIL SEDs, where the volume weights are obtained from our sampling strategy.

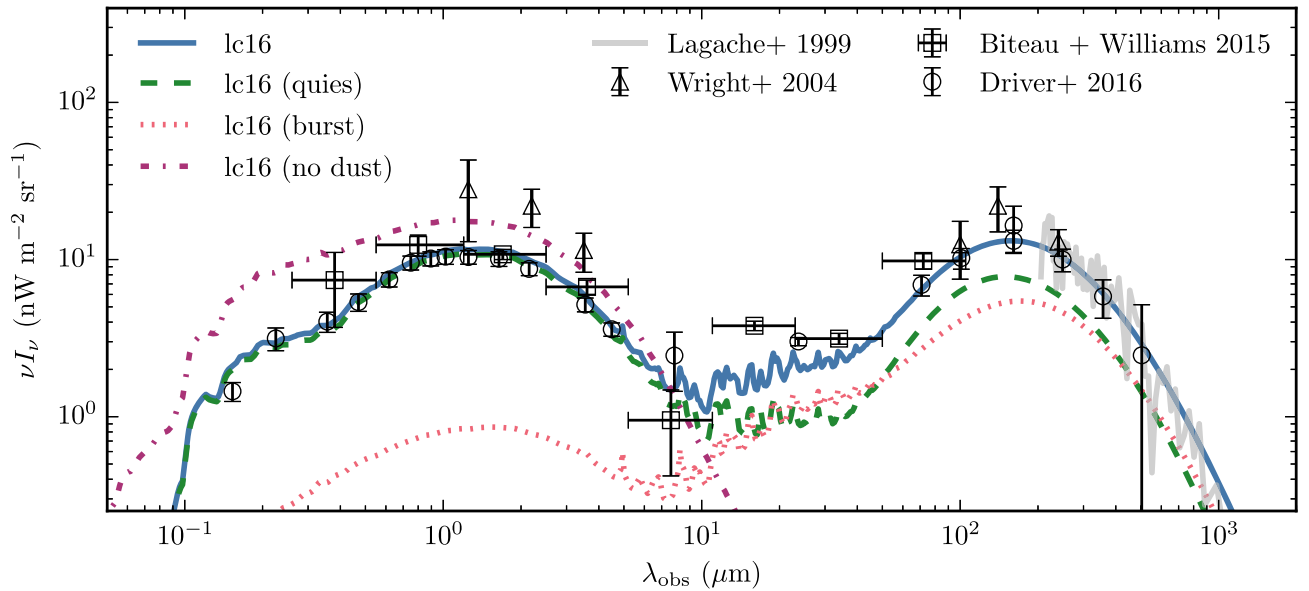


Figure 2. Predicted intensity of UV-to-mm EBL (solid blue line). The contributions from quiescent and starburst galaxies are shown as dashed green and dotted red lines respectively. The EBL without the effects of dust absorption and emission is shown as the dash-dotted magenta line. Observational data are from Lagache et al. (1999, direct detection), Wright (2004, direct detection), Biteau & Williams (2015, TeV photon scattering), and Driver et al. (2016, integrated number counts).

estimates from galaxy number counts (Driver et al. 2016) over those from *COBE* (Wright 2004) at these wavelengths.

The model predictions are in excellent agreement with the observational data over the whole UV-to-mm range, with only minor discrepancies at far-UV ($\sim 0.15 \mu\text{m}$) and mid-IR ($\sim 10\text{--}30 \mu\text{m}$) wavelengths where the model appears to tentatively over- and underpredict the data respectively. We stress that this remarkable agreement is not a result of how the pre-existing model we are using was calibrated (see Lacey et al. 2016 for full details).

The data used for calibration include far-IR number counts at *Herschel*-SPIRE and SCUBA wavelengths (250, 350, 500, and $850 \mu\text{m}$), which tend to be dominated by galaxies with fluxes brighter than those that dominate the background light. This is because the galaxy counts are often determined from confusion-limited imaging at these wavelengths, which makes it difficult to resolve the fainter sources responsible for the bulk of the EBL. Additionally, the model uses the evolution of the rest-frame *K*-band luminosity function up to $z = 3$ as a constraint. However, these luminosity functions span different observer-frame wavelengths at each epoch so it is not clear to what extent they constrain the EBL.

Furthermore, the predicted EBL covers many wavelengths that were not used at all in the model calibration, as the original calibration did not include a full dust grain model and radiative transfer calculation, without which it is not possible to predict mid-IR wavelengths accurately (Cowley et al. 2017). Therefore, this agreement is a genuine success of the model and reflects its predictive power, based on the self-consistent treatment of the physical processes of galaxy formation combined with the radiative transfer of stellar radiation through interstellar dust.

Interestingly, our predictions indicate that emission from quiescent galaxies (i.e. those for which star formation is not dynamically triggered and that form stars according to a solar-neighbourhood IMF) dominates the EBL over the whole UV-to-mm wavelength

range, apart from at $\lambda_{\text{obs}} \sim 30 \mu\text{m}$ (where there is a significant contribution from redshifted PAH emission originating in starburst galaxies) and for $\lambda_{\text{obs}} \gtrsim 350 \mu\text{m}$, where the contribution from both populations is approximately equal. It should also be noted that quiescent galaxies account for almost all of the EBL for $\lambda_{\text{obs}} \lesssim 8 \mu\text{m}$, whereas bursts make a more significant contribution at longer wavelengths. This is unsurprising, as the top-heavy IMF implemented for these galaxies during their dynamically triggered star formation bursts is very efficient at boosting the emission from interstellar dust at these longer wavelengths (Baugh et al. 2005).

Integrating the predicted background light, we find $I_{\text{COB}} = 25.9 \text{ nW m}^{-2} \text{ sr}^{-1}$ (52 percent of the total), $I_{\text{CIB}} = 24.4 \text{ nW m}^{-2} \text{ sr}^{-1}$ (48 percent) using $8 \mu\text{m}$ as the division between the two regimes (see equation 10). This is a very similar distribution of intensity (or brightness) to that found by observational studies (e.g. Hauser & Dwek 2001; Dole et al. 2006), which follows from the agreement of our predictions with the observed EBL spectrum. It indicates that approximately half of the energy emitted by stars over the history of the Universe has been re-radiated by interstellar dust at longer wavelengths, and highlights the importance of understanding dust-obscured star formation for understanding the cosmic star formation history.

Andrews et al. (2018) also briefly compared EBL predictions of the Lacey et al. (2016) and Gonzalez-Perez et al. (2014) GALFORM models to observational data and the predictions of their own model. However, Andrews et al. used a slightly different version of the Lacey et al. (2016) model than in this work, as the one we use here has been re-calibrated for implementation in merger trees from the P-Millennium dark matter simulation. Additionally, the GALFORM photometry in Andrews et al. was computed using the simplified dust model described in Lacey et al. (2016) and not the full radiative transfer calculation with GRASIL. Most of the differences between the Lacey et al. GALFORM EBL predictions at

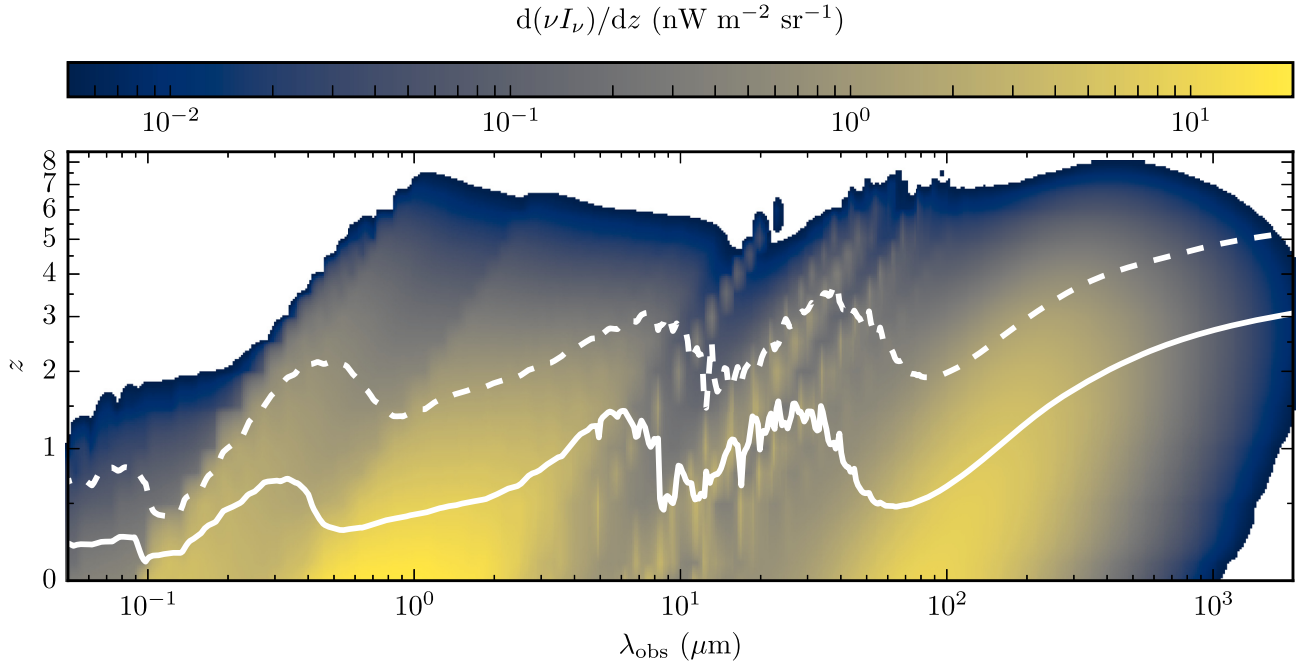


Figure 3. The predicted background light per unit redshift as a function of emission redshift and observer-frame wavelength. The solid line indicates the median redshift i.e. the redshift at which half of the background light at that observed wavelength had been produced. The dashed line indicates the tenth percentile redshift. The ‘cividis’ colourmap used is described by Nuñez et al. (2018).

optical/near-IR wavelengths⁵ presented here and those in Andrews et al. relate to the recalibration of the model, rather than the use of GRASIL. We discuss this in Appendix D.

In Fig. 3 we show the contribution to the $z = 0$ EBL from different emission redshifts. Also shown is the median emission redshift of the EBL as a function of observed wavelength, i.e. the redshift at which 50 per cent of the EBL had been produced at that observed wavelength (solid line), and the redshift at which ten per cent of the EBL had been produced (dashed line). From this we can see that most of the EBL is produced at $z \lesssim 1$, except at $\lambda_{\text{obs}} \gtrsim 100 \mu\text{m}$, where it comes from increasingly higher redshifts as a function of increasing observed wavelength. This is a result of the negative k -correction (e.g. Blain et al. 2002; Casey, Narayanan & Cooray 2014) that this portion of a galaxy SED experiences. It should also be noted that the median redshift is not generally a monotonic function of wavelength, but that there are various maxima that can be related to features in the redshifted SEDs of galaxies. For example, the peak at $\lambda_{\text{obs}} \sim 0.3 \mu\text{m}$ falls between the Lyman and 4000 Å breaks, the peak at $\lambda_{\text{obs}} \sim 5 \mu\text{m}$ is caused by emission from old stars and the peak (and smaller features within) around $\lambda_{\text{obs}} \sim 30 \mu\text{m}$ can be attributed to PAH emission.

3.2 Galaxy number counts and the emission redshift distribution of the EBL

As we have established the agreement between our model predictions for the EBL and current observations, it is worth investigating the agreement between the predicted and measured galaxy number counts since the background light is equal to the flux-weighted

integral of the galaxy number counts, provided that all of it is emitted from galaxies. We show our predictions compared to the observational data compiled by Driver et al. (2016) for a range of bands covering the UV-to-mm in the main panels of Fig. 4. The figures for other bands are shown in Appendix A. We have weighted the number counts by flux in these panels such that the integral under the curve with respect to the (logarithm of the) abscissa is equal to the EBL in that band (see equation 7). It also allows a clear visual indication of the galaxy fluxes that contribute most to the EBL at different wavelengths.

The agreement between our model predictions and observations is very good over the whole wavelength range. There are some small discrepancies, however. The GALEX-FUV counts appear to be overpredicted. The model also appears to underpredict the peak in the counts at $\sim 10^{-1}$ mJy in the IRAC-8 μm and MIPS-24 μm filters. These differences are related to the minor discrepancies seen in Fig. 2.

We note that the flux-weighted number counts in the SPIRE-500 μm filter peak at around 1 mJy, which roughly coincides with the faintest observational data available, and that a significant proportion of the EBL comes from fainter galaxies. These faint data points are from Béthermin et al. (2012), who used a stacking analysis to derive estimates of the galaxy counts below the confusion limit of the *Herschel* imaging. This highlights the point made above that calibrating the model to the bright number counts at these wavelengths does not necessarily guarantee a good agreement with the background light.

The emission redshift distribution of the background light in each band is shown in the minor panels in Fig. 4. We can see here that burst galaxies generally contribute more to the background light at higher redshifts, and indeed dominate the background light at mid-to far-IR wavelengths for $z \gtrsim 2$. A comparison of our predictions for the redshift distribution of the background light with available observational infrared data is shown in Fig. 5. Here we compare the

⁵The GALFORM line segments at $\lambda_{\text{obs}} = 300\text{--}400 \mu\text{m}$ in fig. 9 of Andrews et al. are erroneous and do not relate to the GALFORM model (Andrews et al., private communication).

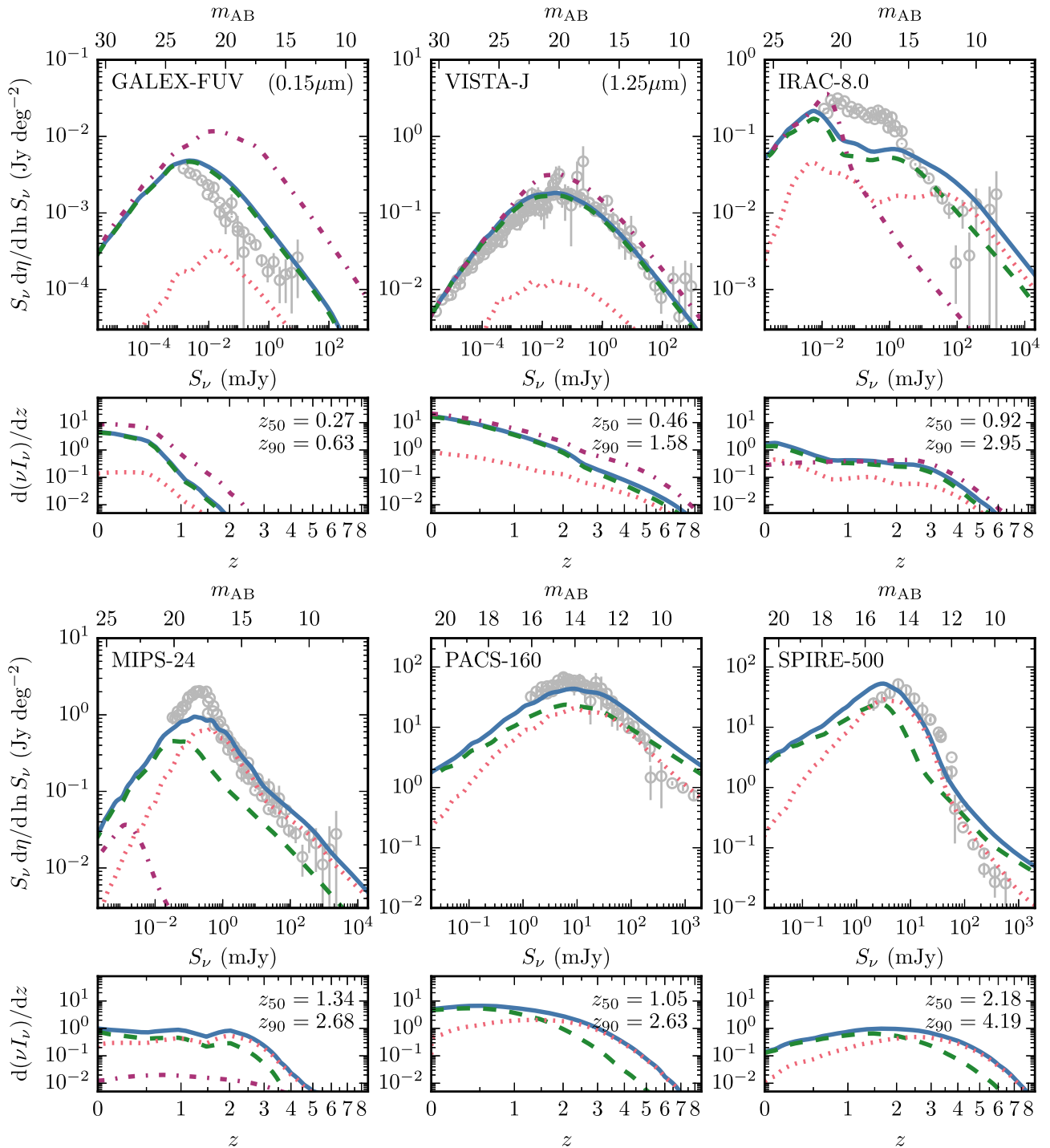


Figure 4. Flux-weighted galaxy number counts (main panels) and distribution of emission redshifts for the background light (in units of $\text{nW m}^{-2} \text{sr}^{-1}$). The bands are indicated in each panel. Lines have the same meaning as in Fig. 2. Observational data (grey points) are from the compilation of Driver et al. (2016). z_{50} and z_{90} correspond to the median and 90th percentile redshifts of the distributions.

observations of Schmidt et al. (2015), derived from cross-correlating *Planck* High-Frequency Instrument maps with quasars identified in the Sloan Digital Sky Survey DR7. We find good agreement over all redshifts, though note that the errorbars on these data are significant.

Additionally, we compare our predictions for the distribution of EBL emission redshifts to the stacked data of Jauzac et al. (2011) and Béthermin et al. (2012). These authors stacked *Herschel* images on the positions of $S_{24\mu\text{m}} > 80 \mu\text{Jy}$ sources with known redshifts.

We include this flux limit in our predictions and find generally good agreement with the observational data (we remind the reader that no infrared data at wavelengths shorter than $250 \mu\text{m}$ was used in the calibration of our fiducial model). Our flux-limited predictions are slightly bi-modal. This is caused by PAH emission being redshifted through the $24 \mu\text{m}$ filter. In this case, the relatively broad peak in the predicted $24 \mu\text{m}$ distribution at $z \sim 2$ is due to the redshifted 7.7 and $8.6 \mu\text{m}$ PAH features originating from starburst galaxies (see

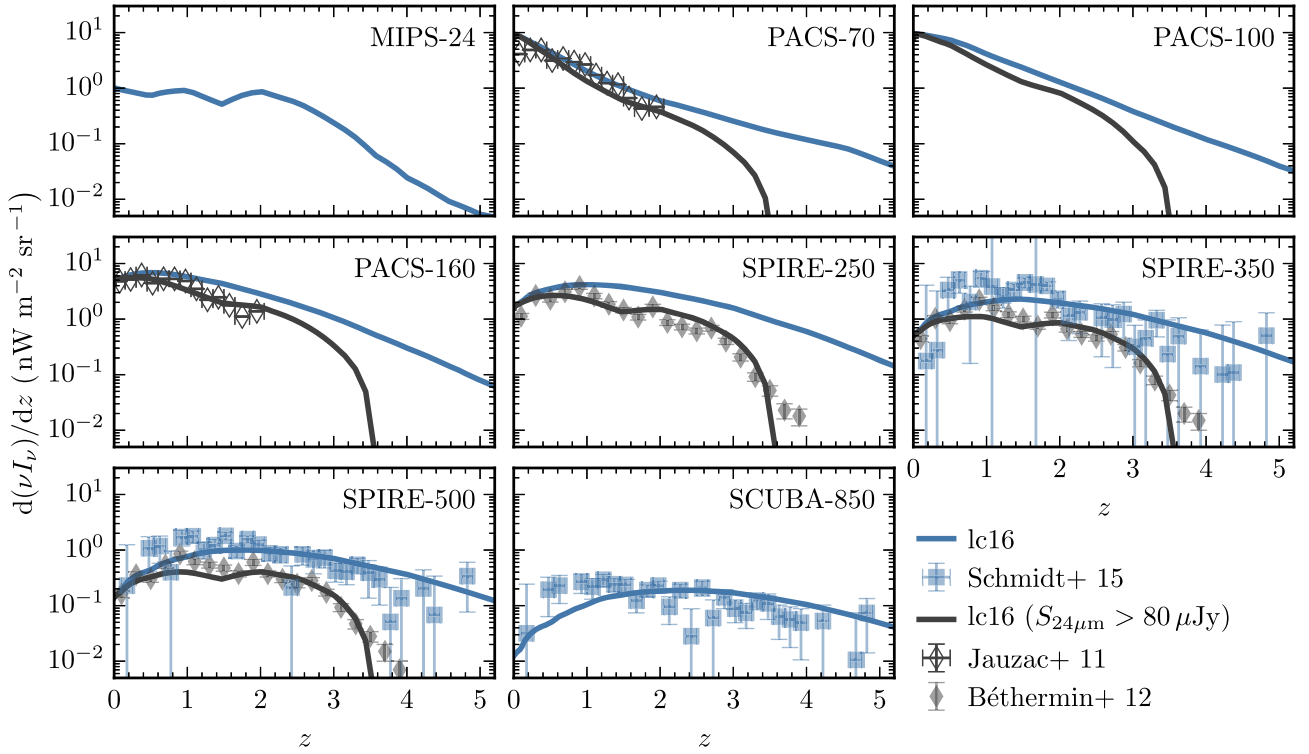


Figure 5. The predicted emission redshift distribution of the background light at far-IR wavelengths for the band indicated in each panel. Our model predictions for all galaxies are the blue solid lines while predictions for galaxies with $S_{24\mu\text{m}} > 80 \mu\text{Jy}$ are shown as dark grey lines. Observational data are from Jauzac et al. (2011, open diamonds), Béthermin et al. (2012, grey diamonds), and Schmidt et al. (2015, blue squares).

also the relevant panel in Fig. 4). Béthermin et al. find some features in their observed distribution that are too ‘sharp’ in redshift to be caused by PAH emission, as the width of the MIPS 24 μm filter causes this to appear over a broad range of redshifts. Instead, as some of these features coincide with known large-scale structures in the COSMOS field (e.g. at $z = 0.3$ and 1.9), they attribute them to cosmic structure, since the COSMOS field is small enough that the sampling variance due to cosmic structure is significant. We do not make specific predictions for the sampling variance here but reiterate that the model is able plausibly to reproduce the build-up of the infrared background light since $z \sim 4$. In Appendix B we also compare our infrared emission redshift distributions to those of Viero et al. (2013), who performed a similar stacking analysis to Jauzac et al. (2011) and Béthermin et al. (2012) but instead stacked on a K -band selected sample and implemented a magnitude limit of $K_{\text{AB}} < 24$ for their procedure. Including this near-IR selection in our predictions we find a similarly good agreement with their data as that seen in Fig. 5 (see Fig. B1).

3.3 The cosmic spectral energy distribution

The cosmic spectral energy distribution (CSED; e.g. Driver et al. 2008; Andrews et al. 2017), ε_ν , describes the luminosity density per unit frequency as a function of wavelength at a given epoch of the Universe’s history (see equation 8). This is related to the EBL, I_ν , which can be derived by integrating the volume-weighted (and redshifted) CSEDs over the history of the Universe (see equation 9).

We show the evolution of our predicted CSEDs in Fig. 6. The optical to near-IR continuum slopes ($\lambda_{\text{rest}} \sim 0.4\text{--}3 \mu\text{m}$) evolve quite dramatically from $z = 8$ to $z \sim 3$, as at these wavelengths the build-up of old stars contributes to a flatter spectrum by $z \sim 3$.

This is independent of dust attenuation, as we can observe a similar evolution in the unattenuated CSEDs. The UV continuum slopes appear to remain fairly blue [i.e. $\beta_{\text{UV}} \sim -2$ if we fit the far-UV ($0.1 \mu\text{m} < \lambda_{\text{rest}} < 0.3 \mu\text{m}$) portion of the CSED with a power law, $\varepsilon_\nu \propto \lambda^{2+\beta_{\text{UV}}}$] at all redshifts, which may contribute in part to the overprediction of the EBL at far-UV wavelengths. The far-IR emission is dominated by burst galaxies for $z \gtrsim 2$, and they continue to play a prominent role in the average PAH emission until $z \sim 0.5$, but never make a significant contribution at shorter wavelengths due to a greater dust attenuation in bursts.

We compare our predictions to the observational estimates of Andrews et al. (2017) for $z < 0.8$, where our simulation snapshots coincide with their redshift bins. Andrews et al. estimated the CSED by summing fitted SEDs based on MAGPHYS templates (da Cunha, Charlot & Elbaz 2008) and photometry from the Galaxy and Mass Assembly survey (Driver et al. 2011) for $0.02 < z < 0.2$ and the G10 region of the Cosmic Evolution Survey (COSMOS, Scoville et al. 2007) for $0.2 < z < 1.0$. Andrews et al. assume a standard solar neighbourhood IMF in their analysis. We do not expect that this choice will have a significant impact on the CSED they recover, however, as observations over a wide range of wavelengths are used to constrain the SED fitting, including the far-infrared and sub-millimetre range.⁶ Here we show their strict lower and upper bounds [columns labelled (1) and (3)

⁶The choice of IMF will, however, have an effect on the values of the derived physical parameters, such as the star formation rate, in the models used by Andrews et al. Our main interest is in the form of the CSED that they recover, and since this is constrained to match observations over the UV-mm wavelength range it should not be strongly affected by the choice of IMF.

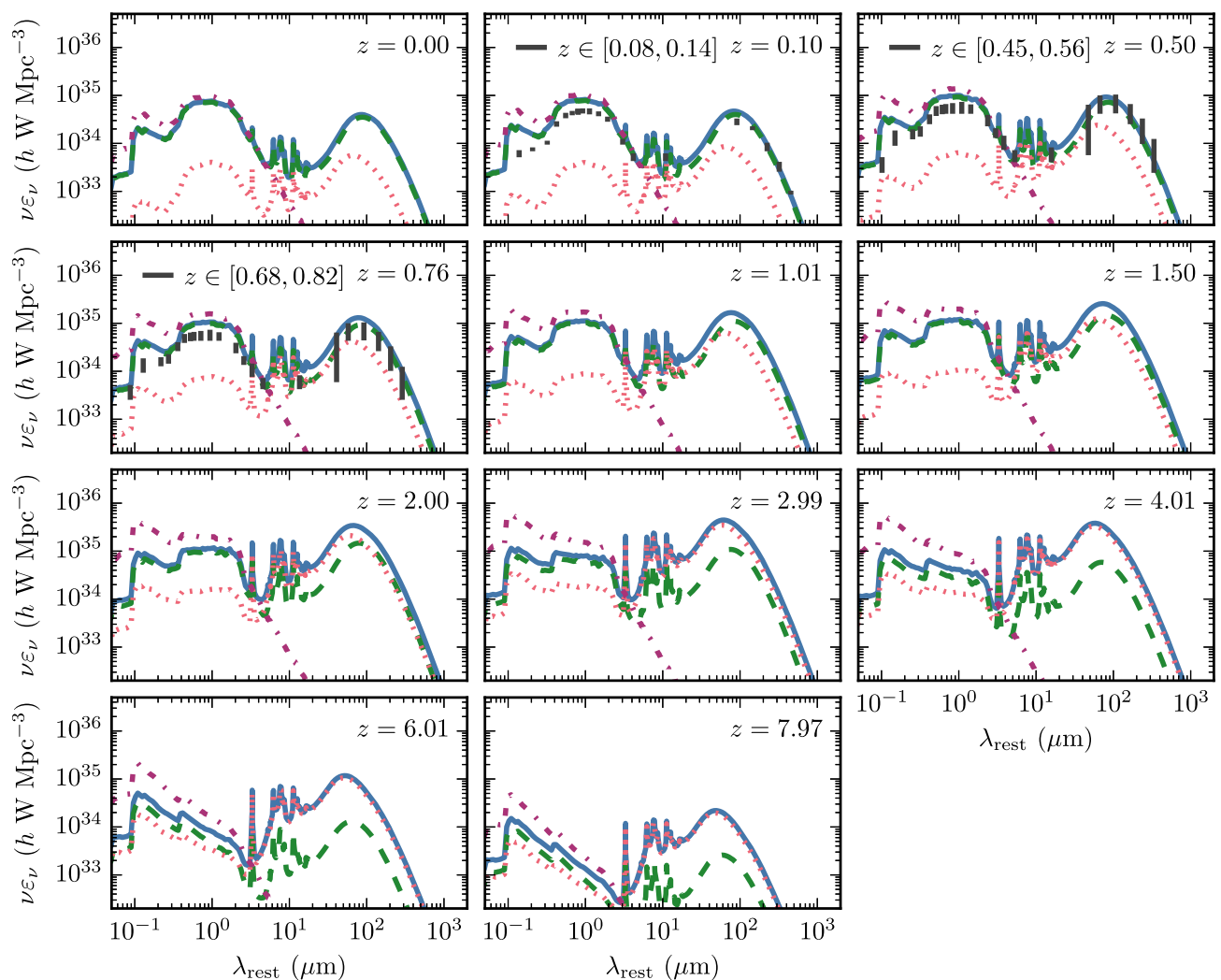


Figure 6. The predicted CSED at the redshift indicated in the panel. Model lines have the same meaning as in Fig. 2. Observational data at $z < 0.8$, shown as dark-grey bars, are from Andrews et al. (2017); the redshift range covered by these data is indicated in each panel.

respectively in their tables 1 and 2], which are respectively the V_{\max} corrected sum of their galaxy MAGPHYS SEDs and the V_{\max} corrected sum with a spline-based optical luminosity completeness correction and upper limits included. There is generally good agreement between our predictions and the Andrews et al. estimates, particularly in the far-IR. The model, however, does seem to mildly overpredict the optical emission in this redshift range, and the predicted UV continuum slopes appear to be too steep (i.e. too blue) relative to observations, which is probably connected to our overprediction of the GALEX-FUV number counts seen in Fig. 4.

3.4 The importance of a top-heavy IMF

We now investigate the extent to which the ability to reproduce the EBL relies on the top-heavy IMF assumed for dynamically-triggered star formation in our model. In doing so we reassess the argument first put forward by Fardal et al. (2007), namely that the present-day stellar mass density, the cosmic star formation history and the EBL are not consistent with one another if a uniform solar-neighbourhood IMF is assumed. Fardal et al. argued that an IMF that is ‘paunchy’ on average, containing an excess

of stars in the range $1 < m < 8 M_{\odot}$ (see their table 1 for a precise definition), is most favoured by these observational constraints.

Here we investigate this using our model. As the form of the IMF is an assumption made in observational estimates of physical properties such as stellar mass and star formation rate, and that is precisely what we are trying to investigate here, we compare only to directly observable properties. As a proxy for local stellar mass density we use the K -band luminosity function at $z = 0$ (see the comparison of the predictions of the fiducial model and the two variants considered here with observational estimates in Fig. 1)⁷ and for the cosmic star formation history we use the data compilation of Madau & Dickinson (2014). However, in the latter case, rather than comparing the star formation rates predicted directly by our model, we compute the predicted IR (8–1000 μm) and attenuated far-UV luminosity densities (ρ_{IR} and $\rho_{\text{FUV,atten}}$, respectively) and convert these into apparent star formation rates

⁷We stress that the K -band luminosity function shown in Fig. 1 was assigned the most weight, amongst various observational constraints, in calibrating the fiducial model.

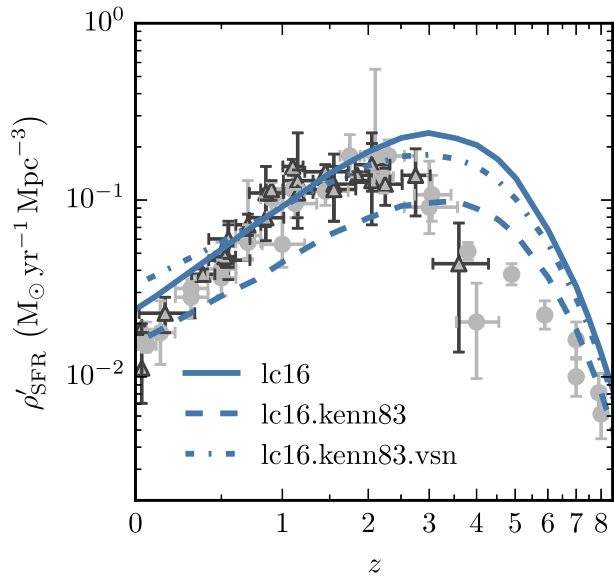


Figure 7. The apparent cosmic star formation history. Model predictions are from the fiducial model (lc16, solid line), a variant with a universal Kennicutt (1983) IMF (lc16.kenn83, dashed line) and a variant with a universal IMF and a lower supernovae feedback mass-loading normalization (lc16.kenn83.vsn, dot-dashed line). Cosmic star formation history data are as compiled by Madau & Dickinson (2014), data from UV and far-IR surveys are shown as light grey circles and light grey triangles with a darker outline, respectively. The model predictions for ρ'_{SFR} are calculated using equation (11).

using the same conversion factors as Madau & Dickinson (see their equation 12) i.e.

$$\rho'_{\text{SFR}} = \kappa_{\text{FUV}} \rho_{\text{FUV,atten}} + \kappa_{\text{IR}} \rho_{\text{IR}}, \quad (11)$$

where $\kappa_{\text{FUV}} = 1.3 \times 10^{-28} M_{\odot} \text{ yr}^{-1} \text{ erg}^{-1} \text{ s Hz}$ and $\kappa_{\text{IR}} = 4.5 \times 10^{-44} M_{\odot} \text{ yr}^{-1} \text{ erg}^{-1} \text{ s}$, which are derived for a Salpeter IMF with $0.1 < m < 100 M_{\odot}$. This is not the same as the intrinsic star formation rate density predicted by GALFORM, which is why we use the prime symbol, ', to denote the apparent cosmic star formation history, ρ'_{SFR} , in equation (11). This is discussed in more detail in Appendix C.

Our model predictions for the apparent star formation rate density are compared to observational data in Fig. 7 which shows that the model can reproduce the cosmic star formation rate density reasonably well for $z \lesssim 2.5$. The variant with a universal IMF and the same SN feedback as the fiducial model underpredicts the apparent star formation rate density at $z < 2$. The variant with reduced SN feedback gives a similar prediction to the fiducial model. The fiducial model appears to overpredict the observational data at higher redshifts. However, in this redshift regime the data are highly uncertain, as most of the observational constraints come from far-UV luminosity functions and so are sensitive to assumptions made about dust attenuation and also typically involve large extrapolations of observed far-UV luminosity functions to fainter magnitudes than actually probed by the data. According to our model, the apparent star formation rate density at these redshifts is dominated by dust-obscured star formation (see Fig. C1). Complementary far-IR observations are extremely challenging at these redshifts, as the coarse angular resolution of single-dish telescopes used for imaging surveys at these wavelengths means that it is only possible to resolve the most highly star-forming objects. It is therefore possible that a significant amount of infrared luminosity density is currently

unaccounted for at $z \gtrsim 3$ (e.g. Rowan-Robinson et al. 2016), though this conclusion remains controversial (e.g. Bouwens et al. 2015; Finkelstein et al. 2015; Bouwens et al. 2016; Dunlop et al. 2017).

Fig. 8 compares the predictions of the fiducial model and the two variants with a universal IMF to the observational estimates of the EBL. The variant with a universal IMF and the same SN feedback as the fiducial model (lc16.kenn83) does not match the EBL observations as well as the fiducial one. Beyond $10 \mu\text{m}$, this variant model underpredicts the EBL by a factor of three. The variant with reduced SN feedback (lc16.kenn83.vsn) fares better at these long wavelengths. However, this model overpredicts the EBL in the near-infrared, optical, and ultra-violet. Here, we remind the reader that it is most appropriate to compare our predictions with the galaxy count-based estimates of Driver et al. (2016). The two variants considered here therefore predict the wrong shape for the EBL.

Whilst a more detailed parameter space exploration might yield better fitting universal IMF variant models (here we have only considered varying a single parameter), it appears unlikely that they will be able to achieve as good a level of agreement as our fiducial model. In any case, the difficulties of universal IMF models in reproducing the observed abundance of bright sub-mm galaxies (whilst simultaneously reproducing other observational data) will almost certainly remain. Reproducing the abundance of bright sub-mm galaxies (e.g. Smail et al. 1997; Hughes et al. 1998) was the primary reason a top-heavy IMF was originally introduced into the GALFORM model by Baugh et al. (2005). A top-heavy IMF is extremely efficient at boosting a galaxy's sub-mm flux as: (i) more massive stars are formed per unit star formation so that the intrinsic UV luminosity is increased; and (ii) more metals and hence interstellar dust are produced through an increased supernova rate with which to absorb and re-radiate the increased amount of UV radiation at sub-mm wavelengths. Whilst the current model assumes a less top-heavy IMF than used by Baugh et al. we highlight that this feature is still necessary for this purpose in Fig. 9, showing the number counts of sub-mm galaxies for the different models. The universal IMF variants dramatically fail to reproduce the abundance of bright ($\sim 1\text{--}10 \text{ mJy}$) sub-mm galaxies by around an order of magnitude, and it is difficult to see how further reducing the impact of feedback mechanisms in the model would solve this problem without the predictions becoming inconsistent with the $z = 0$ distribution of K -band light.

We add that this is not a difficulty unique to the GALFORM model, but is shared by other semi-analytical models (e.g. Somerville et al. 2012) and hydrodynamical simulations (e.g. EAGLE: Crain et al. 2015; Schaye et al. 2015), as is shown in the bottom panel of Fig. 9. The Somerville et al. IR luminosities were predicted using the observationally calibrated dust emission templates of Rieke et al. (2009). The EAGLE luminosities were computed using the radiative transfer code SKIRT (e.g. Baes et al. 2011) as described in Camps et al. (2018) and are publicly accessible via the EAGLE database⁸ (McAlpine et al. 2016). We recognize that there are some models in the literature that claim to be able to simultaneously reproduce the sub-mm number counts as well as other observables such as the present-day galaxy stellar mass function using a universal IMF (e.g. Safarzadeh, Lu & Hayward 2017), and we discuss these claims in more detail in Appendix E.

Although still seen as controversial, there is a growing body of observational evidence that supports not only a non-universal

⁸<http://icc.dur.ac.uk/Eagle/database.php>

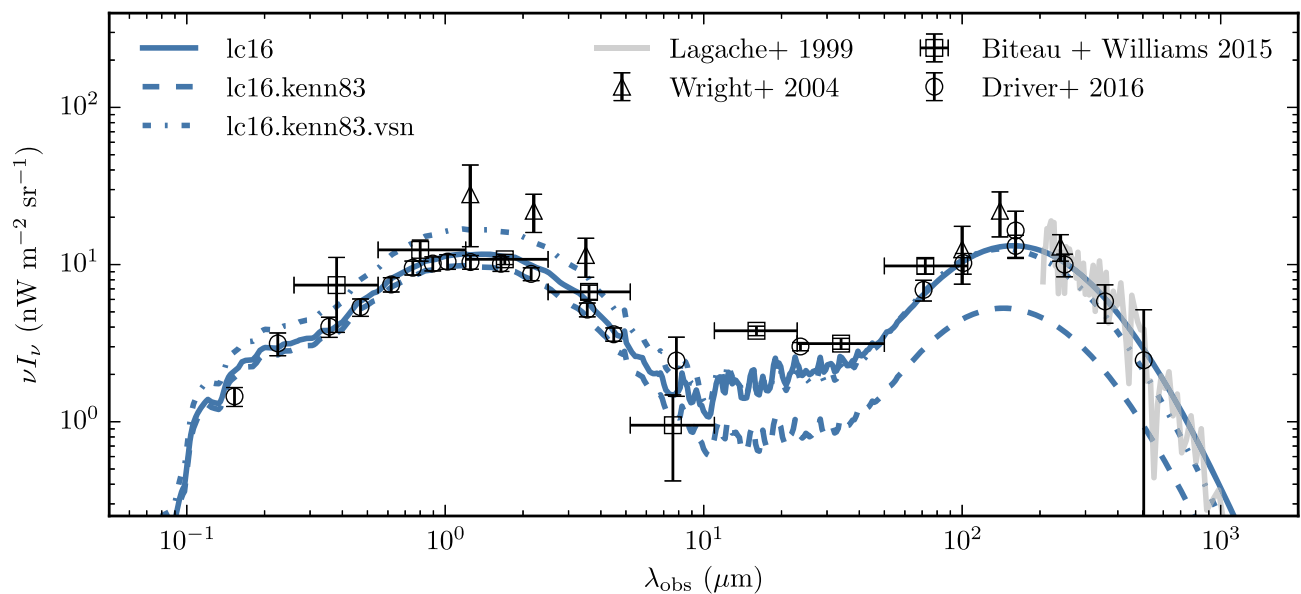


Figure 8. The EBL. Model predictions are from the fiducial model (lc16, solid line), a variant with a universal Kennicutt (1983) IMF (lc16.kenn83, dashed line) and a variant with a universal IMF and a lower supernovae feedback mass-loading normalization (lc16.kenn83.vsn, dash-dotted line). EBL data are as in Fig. 2.

IMF, but the value of the IMF slope proposed by the fiducial model in highly star-forming galaxies (e.g. Finkelstein et al. 2011; Gunawardhana et al. 2011; Romano et al. 2017; Schneider et al. 2018a; Zhang et al. 2018), as discussed in Section 2.2.1.

4 SUMMARY

We have investigated the EBL predicted by the semi-analytical galaxy formation model GALFORM. The model is implemented in halo merger trees from the P-Millennium, a large (800 Mpc)³ cosmological N -body simulation (Baugh et al. 2019) run with cosmological parameters consistent with the *Planck* satellite data, and is calibrated to reproduce an unprecedentedly large set of observational data at $z \lesssim 6$ (Lacey et al. 2016). For computing simulated galaxy SEDs accounting for the absorption and re-emission of stellar radiation by interstellar dust we combined GALFORM with the fully self-consistent radiative transfer code GRASIL (Silva et al. 1998).

The predicted EBL is in remarkable agreement with available observations over the whole of the UV-to-mm range investigated. We show that most (c. 90 per cent) of the EBL is produced at $z \lesssim 2$, although far-IR EBL photons tend to be produced at slightly higher redshifts. Comparing the model predictions for galaxy number counts with observations, we find that the model can generally reproduce the observed distribution of fluxes well over the whole range of wavelengths. We also find that the redshift distribution of the EBL is in good agreement with observational estimates at far-IR wavelengths, and this is also the case if 24 μm and near-IR flux limits on stacked data are considered. We show the predicted evolution of the cosmic SED, the luminosity density as a function of wavelength at a given epoch in the Universe’s history. We find that this is in good agreement with available observational data at $z \lesssim 1$, although the predicted UV continuum slopes appear to be too ‘blue’ at these redshifts, and the luminosity density in the optical ($\lambda_{\text{rest}} \sim 0.3\text{--}4 \mu\text{m}$) portion of the spectrum appears to be mildly overpredicted, perhaps as a

consequence of having slightly too much star formation at higher redshifts.

Finally, we investigated the necessity of a top-heavy IMF during dynamically triggered star formation for reproducing the EBL, simultaneously with the K -band luminosity function at $z = 0$, the cosmic star formation history and the number counts and redshift distribution of galaxies at 850 μm , by examining the predictions of variant models with a universal IMF and comparing these with the predictions of our fiducial model. We find that variant models with a universal solar-neighbourhood IMF struggle to reproduce these observational constraints to the same level of accuracy. In particular, the universal IMF variants do not reproduce the sub-mm (850 μm) galaxy number counts as well as our fiducial model, failing by over an order of magnitude. This is a challenge shared by other physical galaxy formation models. Whilst we have only investigated a small number of variant models with a universal IMF it is difficult to see how simple parameter variations in current models can alleviate this *mismatch whilst simultaneously* reproducing constraints such as the K -band luminosity function at $z = 0$. Similar conclusions were reached by Somerville et al. (2012) who, using a different semi-analytical model of galaxy formation, were unable to reproduce the counts of galaxies at 850 μm using a model with a universal IMF. Thus it seems that these data favour a top-heavy IMF in highly star-forming galaxies, a feature which remains controversial but for which there is mounting evidence from independent observational probes (e.g. Zhang et al. 2018).

The overall excellent agreement of the predictions of our pre-existing galaxy formation model with EBL data is a remarkable success of the model. These data encode multiple aspects of the galaxy formation process and are distinct from the data originally used to calibrate the fiducial model originally. No model parameters were adjusted for the comparisons presented in this study. This work highlights the predictive power and realism of this self-consistent multiwavelength physical model and underlines its utility as a powerful tool for interpreting and understanding multiwavelength observational data over a broad range of redshifts.

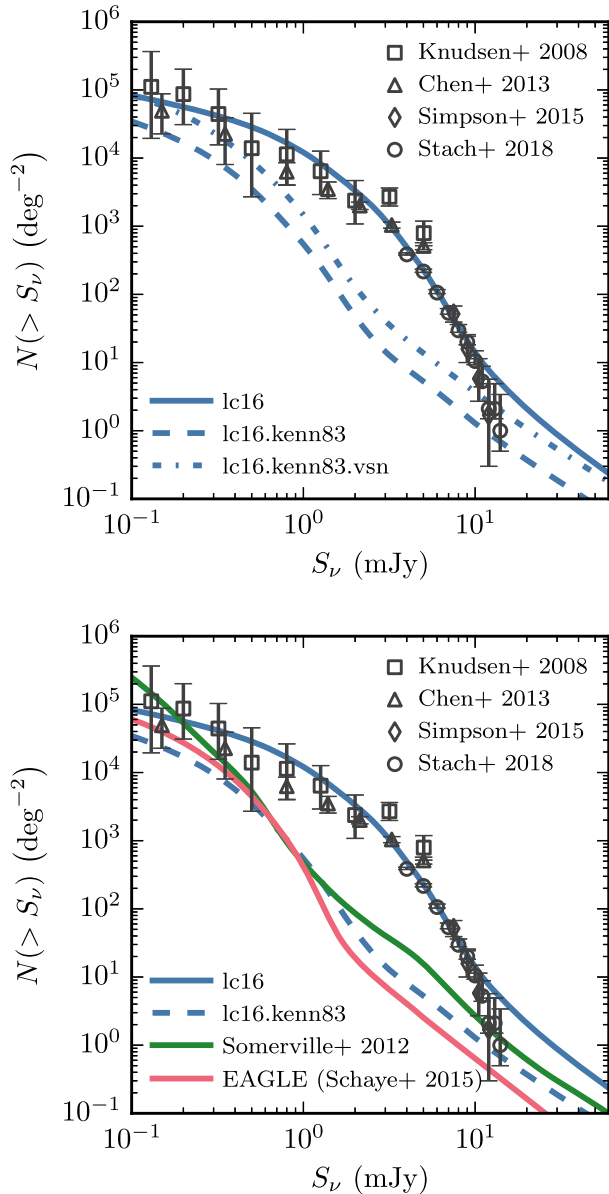


Figure 9. Predicted galaxy number counts at 850 μm . Model lines in the top panel are as in Fig. 8. Lensed single-dish observational data are from Knudsen et al. (2008, squares) and Chen et al. (2013, triangles) and are shown only for $S_{850\mu\text{m}} \leq 5$ mJy. Interferometric data are from Simpson et al. (2015, diamonds) and Stach et al. (2018, circles). In the bottom panel the predictions from the Somerville et al. (2012, green line) semi-analytical model and EAGLE hydrodynamical simulation (Schaye et al. 2015, red line) are also shown.

ACKNOWLEDGEMENTS

The authors would like to thank Alessandro Bressan, Gian-Luigi Granato, and Laura Silva for use of, and discussions relating to, the GRASIL code. Additionally, we would like to acknowledge technical assistance from Joseph Earl, Lydia Heck, John Helly, and Luiz Felipe Rodrigues and helpful discussions with Marta Silva and Lingyu Wang. This work has made use of the open-source PYTHON packages: NUMPY (van der Walt, Colbert & Varoquaux 2011), SCIPY (Oliphant 2007), MATPLOTLIB (Hunter 2007), and IPYTHON (Pérez & Granger 2007). The colour-vision-deficiency-friendly colours used throughout can be found at <https://personal.sron.nl/~pault/>. WIC

acknowledges financial support through the European Research Council Consolidator Grant ID 681627 BUILDUP. This work was supported by the Science and Technology Facilities Council [ST/K501979/1, ST/L00075X/1]. CSF acknowledges an ERC Advanced Investigator Grant, COSMIWAY [GA 267291] and the Science and Technology Facilities Council [ST/F001166/1, ST/I00162X/1]. CdPL has received funding from a Discovery Early Career Researcher Award (DE150100618) and the ARC Centre of Excellence for All Sky Astrophysics in 3 Dimensions (ASTRO 3D), through project number CE170100013. This work used the DiRAC@Durham facility managed by the Institute for Computational Cosmology on behalf of the STFC DiRAC HPC Facility (www.dirac.ac.uk). The equipment was funded by BEIS capital funding via STFC capital grants ST/P002293/1, ST/R002371/1, and ST/S002502/1, Durham University and STFC operations grant ST/R000832/1. DiRAC is part of the National e-Infrastructure. The EAGLE simulations were performed using the DiRAC-2 facility at Durham, managed by the ICC, and the PRACE facility Curie based in France at Très Grand Centre de Calcul, CEA, Bruyères-le-Château.

REFERENCES

- Agladze N. I., Sievers A. J., Jones S. A., Burlitch J. M., Beckwith S. V. W., 1996, *ApJ*, 462, 1026
- Aharonian F. et al., 2006, *Nature*, 440, 1018
- Ahnen M. L. et al., 2016, *A&A*, 590, A24
- Almaini O., Lawrence A., Boyle B. J., 1999, *MNRAS*, 305, L59
- Andrews S. K. et al., 2017, *MNRAS*, 470, 1342
- Andrews S. K., Driver S. P., Davies L. J. M., Lagos C. d. P., Robotham A. S. G., 2018, *MNRAS*, 474, 898
- Arendt R. G. et al., 1998, *ApJ*, 508, 74
- Baes M., Verstappen J., De Looze I., Fritz J., Saftly W., Vidal Pérez E., Stalewski M., Valcke S., 2011, *ApJS*, 196, 22
- Baes M., Trčka A., Camps P., Nersesian A., Trayford J., Theuns T., Dobbels W., 2019, *MNRAS*, 484, 4069
- Ballero S. K., Kroupa P., Matteucci F., 2007, *A&A*, 467, 117
- Barber C., Crain R. A., Schaye J., 2018, *MNRAS*, 479, 5448
- Bastian N., Covey K. R., Meyer M. R., 2010, *ARA&A*, 48, 339
- Baugh C. M., Lacey C. G., Frenk C. S., Granato G. L., Silva L., Bressan A., Benson A. J., Cole S., 2005, *MNRAS*, 356, 1191
- Baugh C. M. et al., 2019, *MNRAS*, 483, 4922
- Bernard J. P., Boulanger F., Desert F. X., Giard M., Helou G., Puget J. L., 1994, *A&A*, 291, L5
- Bernstein R. A., Freedman W. L., Madore B. F., 2002, *ApJ*, 571, 85
- Berta S. et al., 2011, *A&A*, 532, A49
- Béthermin M. et al., 2012, *A&A*, 542, A58
- Bigiel F. et al., 2011, *ApJ*, 730, L13
- Biteau J., Williams D. A., 2015, *ApJ*, 812, 60
- Blain A. W., Smail I., Ivison R. J., Kneib J.-P., Frayer D. T., 2002, *Phys. Rep.*, 369, 111
- Boudet N., Mutschke H., Nayral C., Jäger C., Bernard J.-P., Henning T., Meny C., 2005, *ApJ*, 633, 272
- Bourne N. et al., 2017, *MNRAS*, 467, 1360
- Bouwens R. J. et al., 2015, *ApJ*, 803, 34
- Bouwens R. J. et al., 2016, *ApJ*, 833, 72
- Camps P. et al., 2018, *ApJS*, 234, 20
- Carniani S. et al., 2015, *A&A*, 584, A78
- Casey C. M., Narayanan D., Cooray A., 2014, *Phys. Rep.*, 541, 45
- Chen C.-C., Cowie L. L., Barger A. J., Casey C. M., Lee N., Sanders D. B., Wang W.-H., Williams J. P., 2013, *ApJ*, 776, 131
- Cole S., Lacey C. G., Baugh C. M., Frenk C. S., 2000, *MNRAS*, 319, 168
- Cole S. et al., 2001, *MNRAS*, 326, 255
- Collier W. P., Smith R. J., Lucey J. R., 2018, *MNRAS*, 478, 1595
- Cowley W. I., Lacey C. G., Baugh C. M., Cole S., 2015, *MNRAS*, 446, 1784
- Cowley W. I., Lacey C. G., Baugh C. M., Cole S., 2016, *MNRAS*, 461, 1621

- Cowley W. I., Béthermin M., Lagos C. d. P., Lacey C. G., Baugh C. M., Cole S., 2017, *MNRAS*, 467, 1231
- Cowley W. I., Baugh C. M., Cole S., Frenk C. S., Lacey C. G., 2018, *MNRAS*, 474, 2352
- Crain R. A. et al., 2015, *MNRAS*, 450, 1937
- da Cunha E., Charlot S., Elbaz D., 2008, *MNRAS*, 388, 1595
- Dole H. et al., 2006, *A&A*, 451, 417
- Domínguez A. et al., 2011, *MNRAS*, 410, 2556
- Draine B. T., Lee H. M., 1984, *ApJ*, 285, 89
- Driver S. P., Popescu C. C., Tuffs R. J., Graham A. W., Liske J., Baldry I., 2008, *ApJ*, 678, L101
- Driver S. P. et al., 2011, *MNRAS*, 413, 971
- Driver S. P. et al., 2012, *MNRAS*, 427, 3244
- Driver S. P. et al., 2016, *ApJ*, 827, 108
- Dunlop J. S. et al., 2017, *MNRAS*, 466, 861
- Efstathiou G., Lake G., Negroponte J., 1982, *MNRAS*, 199, 1069
- Fardal M. A., Katz N., Weinberg D. H., Davé R., 2007, *MNRAS*, 379, 985
- Farr W. M., Mandel I., 2018, *Science*, 361, aat6506
- Finkelstein K. D. et al., 2011, *ApJ*, 742, 108
- Finkelstein S. L. et al., 2015, *ApJ*, 810, 71
- Finke J. D., Razzaque S., Dermer C. D., 2010, *ApJ*, 712, 238
- Fixsen D. J., Dwek E., Mather J. C., Bennett C. L., Shafer R. A., 1998, *ApJ*, 508, 123
- Fontanot F., De Lucia G., Hirschmann M., Bruzual G., Charlot S., Zibetti S., 2017, *MNRAS*, 464, 3812
- Franceschini A., Rodighiero G., Vaccari M., 2008, *A&A*, 487, 837
- Gargiulo I. D. et al., 2015, *MNRAS*, 446, 3820
- Geach J. E. et al., 2013, *MNRAS*, 432, 53
- Gilmore R. C., Somerville R. S., Primack J. R., Domínguez A., 2012, *MNRAS*, 422, 3189
- González J. E., Lacey C. G., Baugh C. M., Frenk C. S., 2011, *MNRAS*, 413, 749
- Gonzalez-Perez V., Lacey C. G., Baugh C. M., Lagos C. D. P., Helly J., Campbell D. J. R., Mitchell P. D., 2014, *MNRAS*, 439, 264
- Granato G. L., Lacey C. G., Silva L., Bressan A., Baugh C. M., Cole S., Frenk C. S., 2000, *ApJ*, 542, 710
- Gunawardhana M. L. P. et al., 2011, *MNRAS*, 415, 1647
- Guo Q., White S., Angulo R. E., Henriques B., Lemson G., Boylan-Kolchin M., Thomas P., Short C., 2013, *MNRAS*, 428, 1351
- Hatsukade B., Ohta K., Seko A., Yabe K., Akiyama M., 2013, *ApJ*, 769, L27
- Hatsukade B. et al., 2016, *PASJ*, 68, 36
- Hauser M. G., Dwek E., 2001, *ARA&A*, 39, 249
- Hayward C. C., Kereš D., Jonsson P., Narayanan D., Cox T. J., Hernquist L., 2011, *ApJ*, 743, 159
- Hayward C. C., Narayanan D., Kereš D., Jonsson P., Hopkins P. F., Cox T. J., Hernquist L., 2013, *MNRAS*, 428, 2529
- Helly J. C., Cole S., Frenk C. S., Baugh C. M., Benson A., Lacey C., 2003, *MNRAS*, 338, 903
- Hou J., Frenk C. S., Lacey C. G., Bose S., 2016, *MNRAS*, 463, 1224
- Hughes D. H. et al., 1998, *Nature*, 394, 241
- Hunter J. D., 2007, *Comput. Sci. Eng.*, 9, 90
- Inoue Y., Inoue S., Kobayashi M. A. R., Makiya R., Niino Y., Totani T., 2013, *ApJ*, 768, 197
- Jauzac M. et al., 2011, *A&A*, 525, A52
- Jiang L., Helly J. C., Cole S., Frenk C. S., 2014, *MNRAS*, 440, 2115
- Karim A. et al., 2013, *MNRAS*, 432, 2
- Kennicutt Jr. R. C., 1983, *ApJ*, 272, 54
- Knudsen K. K., van der Werf P. P., Kneib J.-P., 2008, *MNRAS*, 384, 1611
- Kochanek C. S. et al., 2001, *ApJ*, 560, 566
- La Barbera F., Vazdekis A., Ferreras I., Pasquali A., Cappellari M., Martín-Navarro I., Schönebeck F., Falcón-Barroso J., 2016, *MNRAS*, 457, 1468
- Lacey C. G. et al., 2016, *MNRAS*, 462, 3854
- Lagache G., Abergel A., Boulanger F., Désert F. X., Puget J.-L., 1999, *A&A*, 344, 322
- Lagos C. D. P., Lacey C. G., Baugh C. M., Bower R. G., Benson A. J., 2011, *MNRAS*, 416, 1566
- Lu Y. et al., 2014, *ApJ*, 795, 123
- Madau P., Dickinson M., 2014, *ARA&A*, 52, 415
- Madau P., Pozzetti L., 2000, *MNRAS*, 312, L9
- Maraston C., 2005, *MNRAS*, 362, 799
- Mather J. C., Fixsen D. J., Shafer R. A., 1993, in Scholl M. S., ed., *Proc. SPIE Conf. Ser. Vol. 2019, Infrared Spaceborne Remote Sensing*, SPIE, Bellingham, p. 168
- Mattila K., 2006, *MNRAS*, 372, 1253
- McAlpine S. et al., 2016, *Astron. Comput.*, 15, 72
- McCullagh N., Norberg P., Cole S., Gonzalez-Perez V., Baugh C., Helly J., 2017, preprint([arXiv:1705.01988](https://arxiv.org/abs/1705.01988))
- Meiksin A., 2005, *MNRAS*, 356, 596
- Mitchell-Wynne K. et al., 2015, *Nat. Commun.*, 6, 7945
- Nelson D. et al., 2018, *MNRAS*, 475, 624
- Nguyen H. T. et al., 2010, *A&A*, 518, L5
- Nuñez J. R., Anderton C. R., Renslow R. S., 2018, *PLoS One*, 13, 1
- Oliphant T. E., 2007, *Comput. Sci. Eng.*, 9, 10
- Oliver S. J. et al., 2010, *A&A*, 518, L21
- Pérez F., Granger B. E., 2007, *Comput. Sci. Eng.*, 9, 21
- Planck Collaboration et al., 2014, *A&A*, 571, A16
- Puget J.-L., Abergel A., Bernard J.-P., Boulanger F., Burton W. B., Desert F.-X., Hartmann D., 1996, *A&A*, 308, L5
- Rieke G. H., Alonso-Herrero A., Weiner B. J., Pérez-González P. G., Blaylock M., Donley J. L., Marcillac D., 2009, *ApJ*, 692, 556
- Romano D., Matteucci F., Zhang Z.-Y., Papadopoulos P. P., Ivison R. J., 2017, *MNRAS*, 470, 401
- Rowan-Robinson M. et al., 2016, *MNRAS*, 461, 1100
- Safarzadeh M., Lu Y., Hayward C. C., 2017, *MNRAS*, 472, 2462
- Salpeter E. E., 1955, *ApJ*, 121, 161
- Schaye J. et al., 2015, *MNRAS*, 446, 521
- Schmidt S. J., Ménard B., Scranton R., Morrison C. B., Rahman M., Hopkins A. M., 2015, *MNRAS*, 446, 2696
- Schneider F. R. N. et al., 2018a, *Science*, 359, 69
- Schneider F. R. N. et al., 2018b, *Science*, 361, aat7032
- Scott K. S. et al., 2012, *MNRAS*, 423, 575
- Scoville N. et al., 2007, *ApJS*, 172, 1
- Silva L., Granato G. L., Bressan A., Danese L., 1998, *ApJ*, 509, 103
- Silva L., Maiolino R., Granato G. L., 2004, *MNRAS*, 355, 973
- Silverberg R. F., Hauser M. G., Boggess N. W., Kelsall T. J., Moseley S. H., Murdock T. L., 1993, in Scholl M. S., ed., *Proc. SPIE Conf. Ser. Vol. 2019, Infrared Spaceborne Remote Sensing*, SPIE, Bellingham, p. 180
- Simha V., Cole S., 2017, *MNRAS*, 472, 1392
- Simpson J. M. et al., 2015, *ApJ*, 807, 128
- Smail I., Ivison R. J., Blain A. W., 1997, *ApJ*, 490, L5
- Smith R. J., Alton P., Lucey J. R., Conroy C., Carter D., 2015, *MNRAS*, 454, L71
- Somerville R. S., Gilmore R. C., Primack J. R., Domínguez A., 2012, *MNRAS*, 423, 1992
- Springel V. et al., 2005, *Nature*, 435, 629
- Stach S. M. et al., 2018, *ApJ*, 860, 161
- van der Walt S., Colbert C., Varoquaux G., 2011, *Comput. Sci. Eng.*, 13, 22
- Viero M. P. et al., 2013, *ApJ*, 779, 32
- Vogelsberger M. et al., 2014, *MNRAS*, 444, 1518
- Wang W.-H. et al., 2017, *ApJ*, 850, 37
- Wang L., Pearson W. J., Cowley W., Trayford J. W., Béthermin M., Gruppioni C., Hurley P., Michalowski M. J., 2019, *A&A*, 624, A98
- White S. D. M., Rees M. J., 1978, *MNRAS*, 183, 341
- Wright E. L., 2004, *New Astron. Rev.*, 48, 465
- Zemcov M. et al., 2014, *Science*, 346, 732
- Zhang Z.-Y., Romano D., Ivison R. J., Papadopoulos P. P., Matteucci F., 2018, *Nature*, 558, 260

APPENDIX A: GALAXY NUMBER COUNTS AND THE EMISSION REDSHIFT DISTRIBUTION OF THE EBL (II)

Fig. A1 shows the predicted number counts and redshift distribution of the background light in bands used by Driver et al. (2016) but

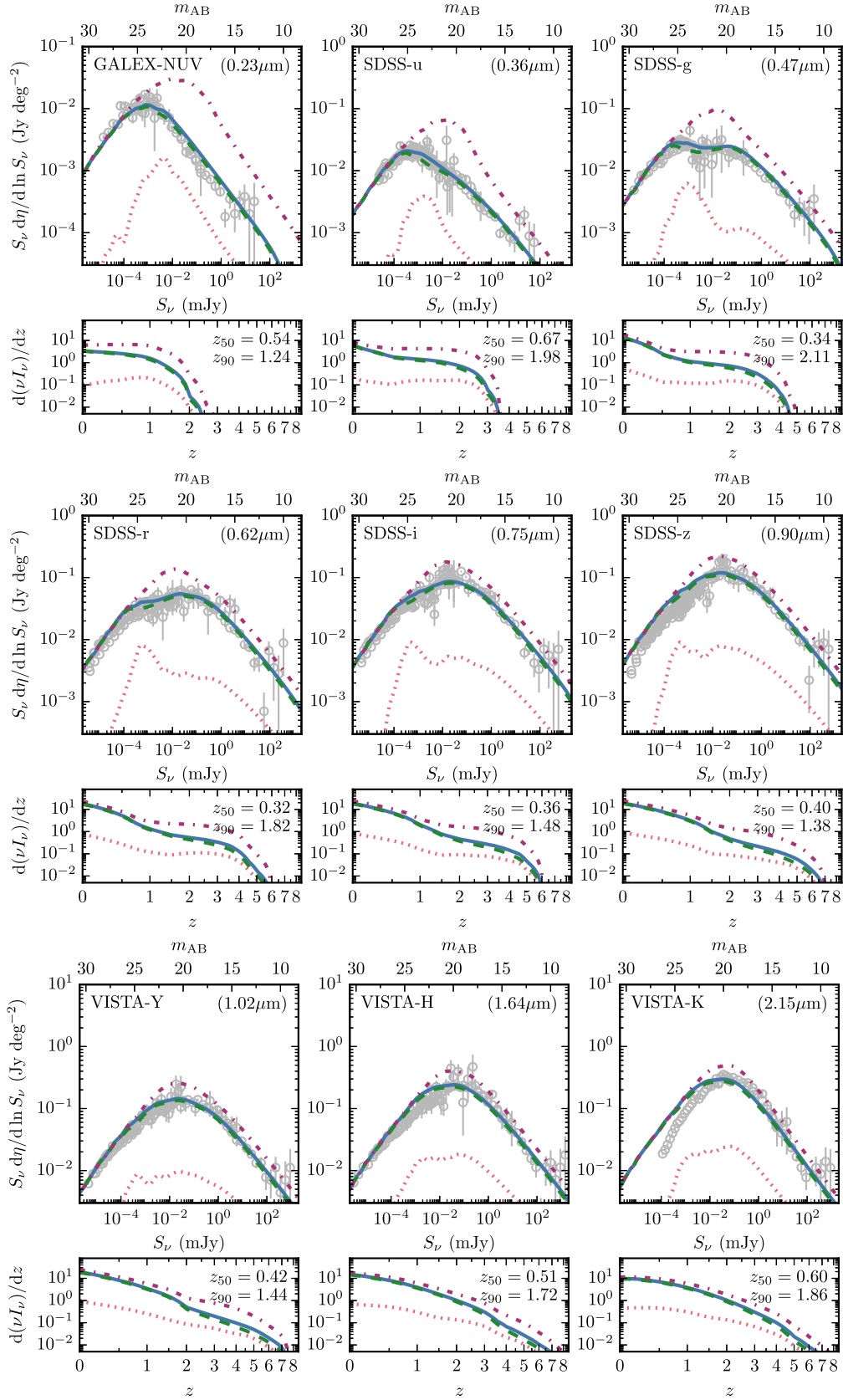


Figure A1. Flux-weighted galaxy number counts (major panels) and redshift distribution of background light (in units of $nW m^{-2} sr^{-1}$) for the band indicated in each panel. Lines have same meaning as in Fig. 2. Observational data are as compiled by Driver et al. (2016). z_{50} and z_{90} correspond to the median and 90th percentile redshifts of the distributions.

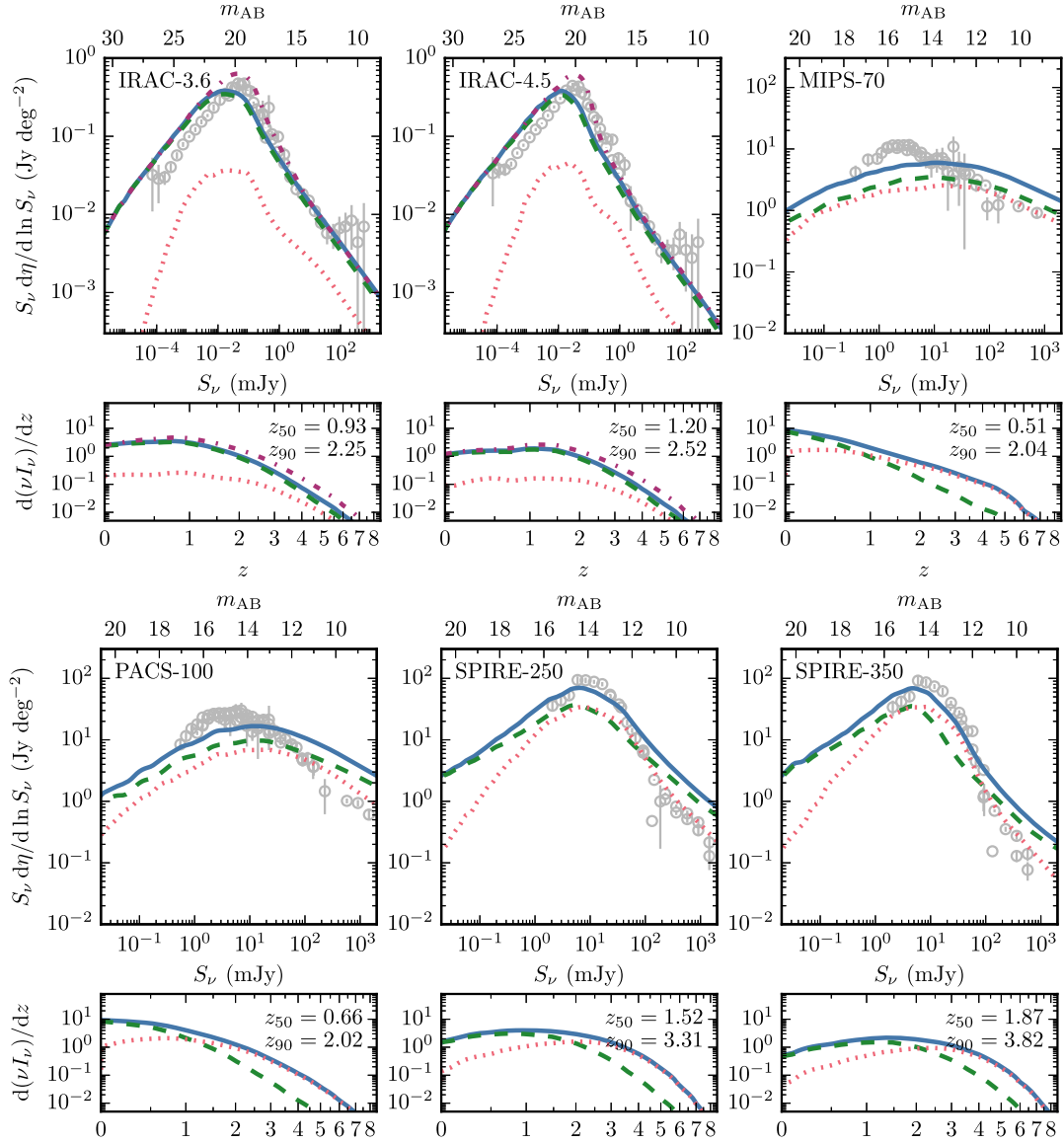


Figure A1 – Continued

not shown in Fig. 4. In Fig. A2 we show these predictions in far-IR bands not considered by Driver et al. Note that in these figures we do not account for the effect that the coarse angular resolution of single-dish telescopes used for imaging surveys

at far-IR wavelengths can have on the derived galaxy number counts (e.g. Karim et al. 2013). The impact this issue has on our model predictions is thoroughly explored in Cowley et al. (2015).

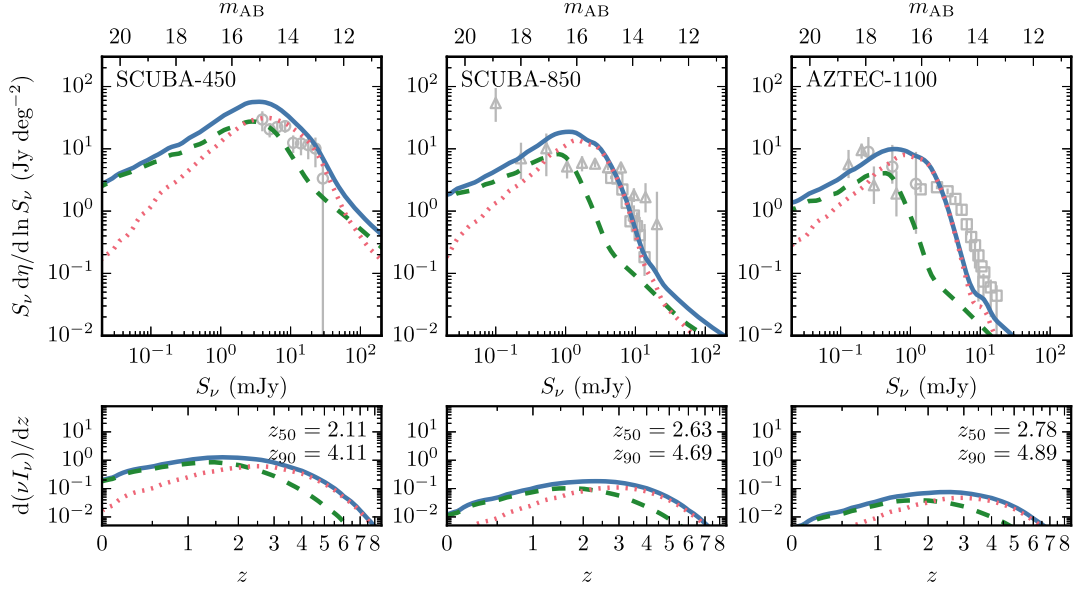


Figure A2. Flux-weighted galaxy number counts (major panels) and redshift distribution of background light (in units of $nW m^{-2} sr^{-1}$) for the band indicated in each panel. Lines have the same meaning as in Fig. 2. Observational data at (i) 450 μm are from Wang et al. (2017); (ii) 850 μm are from Chen et al. (2013, triangles) and Stach et al. (2018, squares); and (iii) 1100 μm are from Scott et al. (2012, squares), Carniani et al. (2015, triangles), and Hatsukade et al. (2016, circles). z_{50} and z_{90} correspond to the median and 90th percentile redshifts of the distributions.

APPENDIX B: THE CONTRIBUTION OF OPTICAL GALAXIES TO THE FAR-INFRARED BACKGROUND

Here we compare our predictions for the distribution of EBL emission redshifts to the observational data of Viero et al. (2013). These authors performed a similar stacking analysis to Jauzac et al. (2011) and Béthermin et al. (2012) on *Herschel* imaging, but began with an input catalogue selected in the near-IR ($K_{AB} < 24$), rather than at 24 μm .

Fig. B1 shows that we find similarly good agreement with these data to that seen in Fig 5. However, it does appear that the model may overestimate the contribution from the lowest redshift bin, particularly at 70 and 100 μm . This is where the volume probed by Viero et al. will be smallest and combined with their modest ~ 0.63 deg 2 area it could be that these lowest-redshift data are not necessarily representative of the Universe. Nevertheless, the overall discrepancy is fairly minor, again showing that the model can plausibly predict the build-up of the EBL at far-IR wavelengths.

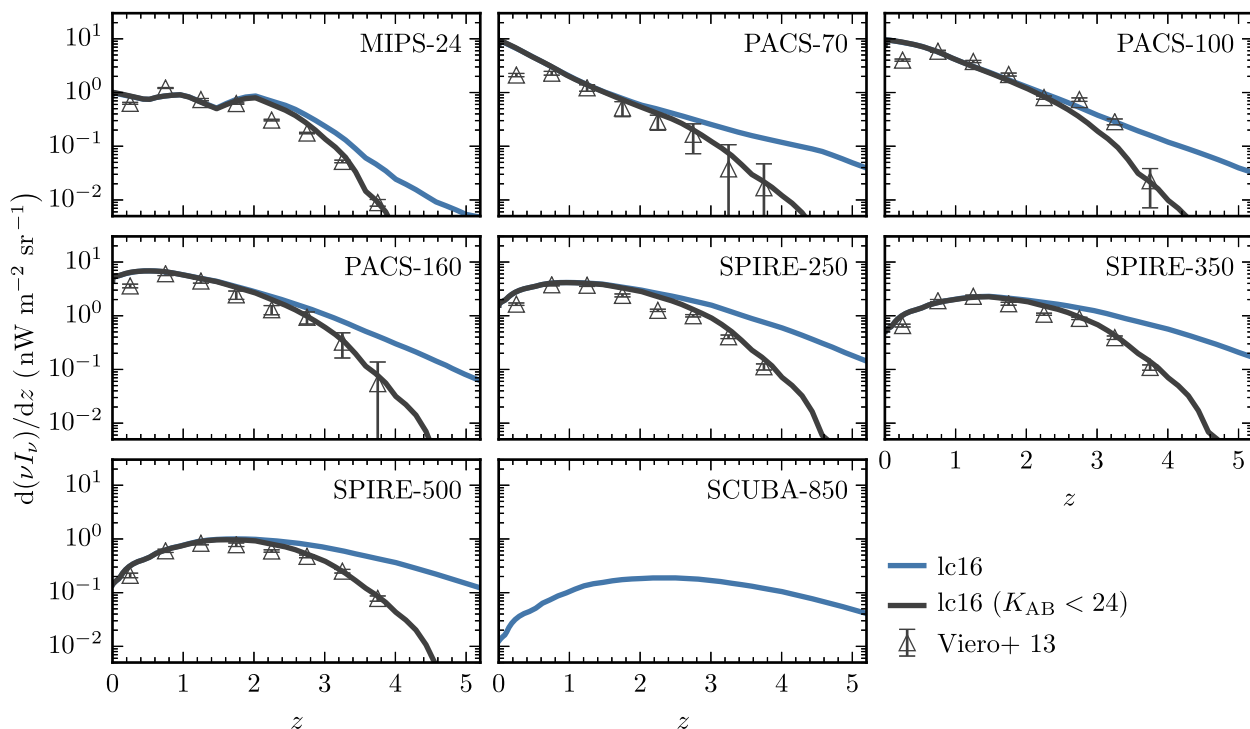


Figure B1. As for Fig. 5, but the dark grey lines now indicate the predictions for galaxies with $K_{AB} < 24$. Observational data are from Viero et al. (2013, open triangles). The estimates of Schmidt et al. have been omitted for clarity.

APPENDIX C: THE COSMIC STAR FORMATION HISTORY

In the top right panel of Fig. 8 we scaled the predicted far-UV and far-IR luminosity densities to apparent star formation rate densities using the same conversion factors as Madau & Dickinson (2014) in order to compare our predictions to their compilation of estimates for the cosmic star formation history (see equation 11). This is not necessarily the same as the intrinsic cosmic star formation history predicted by the model, ρ_{SFR} , and the difference between this and that inferred from equation (11) is shown in the top panel of Fig. C1. The apparent star formation history, ρ'_{SFR} , is a factor of ~ 2 greater than ρ_{SFR} for $z \lesssim 3$. This factor then decreases towards higher redshifts.

In the left-hand panel of Fig. C1 we show the contribution to the total inferred star formation history from the two terms on the right-hand side of equation (11). To ease the comparison with the observational data in this panel we have uncorrected the far-UV

based observational estimates for dust attenuation, using the same method as Madau & Dickinson. The attenuated far-UV luminosity density predicted by the model is in reasonable agreement with the observational data over the whole range of redshifts shown. This is unsurprising as this model has been shown to predict evolution of the rest-frame far-UV luminosity function in good agreement with observational estimates, particularly at high redshifts ($6 \lesssim z \lesssim 10$, Hou et al. 2016; Cowley et al. 2018). The far-IR predictions are in equally reasonable agreement for $z \lesssim 3$, beyond which observational estimates become increasingly challenging as discussed earlier.

Interestingly, the contribution to the apparent star formation history from the far-IR is greater than that from the UV over the entire redshift range shown. This is in contrast to some observational studies (e.g. Bourne et al. 2017; Dunlop et al. 2017), who argue that the UV contribution dominates for $z \gtrsim 4$, though is in agreement with a recent *Herschel* de-blending study (Wang et al. 2019). This again highlights the need for a consensus regarding the dust-obscured star formation rate density at $z \gtrsim 3$.

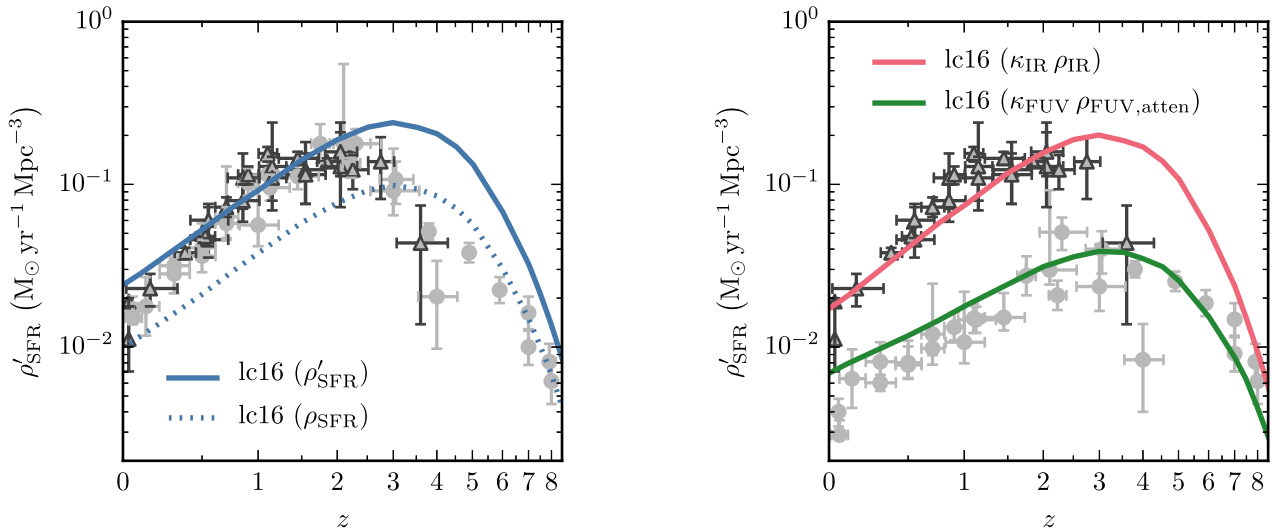


Figure C1. The cosmic star formation history. *Left-hand panel:* the difference between the apparent star formation history inferred using equation (11) (solid line) and the intrinsic prediction of the model (dotted line). *Right-hand panel:* the contribution to the total inferred star formation history from the two terms on the right hand side of equation (11), $\kappa_{\text{FUV}} \rho_{\text{FUV,atten}}$ (green line) and $\kappa_{\text{IR}} \rho_{\text{IR}}$ (red line). Observational data in both panels are from the Madau & Dickinson (2014) compilation, colours and symbols are as in the top-right panel of Fig. 8. In the right-hand panel of this figure we have uncorrected the UV-derived observational estimates for dust attenuation, following the same procedure as Madau & Dickinson.

APPENDIX D: THE IMPACT OF USING GRASIL AND THE RECALIBRATION TO THE P-MILLENNIUM

The model used in this work differs slightly from that originally presented by Lacey et al. (2016) and in this section we discuss the impact these changes have on the predicted EBL.

The halo merger trees in which the galaxy formation model is run have been generated from a new dark matter simulation, the P-Millennium (Baugh et al. 2019), which has different cosmological parameters and a finer halo mass resolution than

the MR7 simulation, which was used by Lacey et al; and an improved prescription for the galaxy merger timescale (Simha & Cole 2017) has been implemented. As a result of these changes, Baugh et al. found it necessary to make small adjustments to two of the galaxy formation parameters such that the original calibration data of Lacey et al. could be reproduced to a similar level of fidelity. As we have stressed earlier, we do not make any further changes to GALFORM’s parameters in this work.

Additionally, here we use GRASIL for predicting galaxy SEDs (see also Cowley et al. 2018), whereas in other GALFORM studies

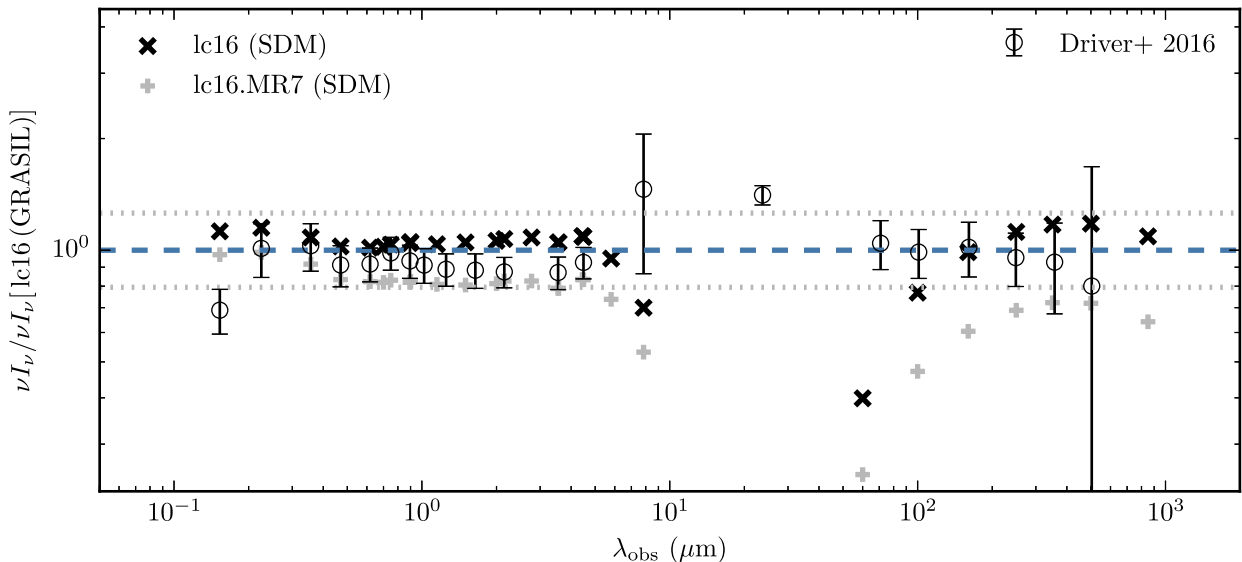


Figure D1. The impact of the P-Millennium recalibration and GRASIL on the predicted EBL. For clarity we have divided everything by the predictions for our fiducial lc16 model with luminosities predicted by GRASIL, i.e. the blue line in Fig. 2. Predictions from our fiducial lc16 model, and the original model presented in Lacey et al. (2016) implemented within halo merger trees from the MR7 simulation, both with luminosities predicted by the simple dust model (SDM) described in Lacey et al. (2016), are shown as black crosses and grey plus signs, respectively. Observational data from Driver et al. (2016, open circles with errorbars) are shown for reference. A blue dashed line at unity and grey dotted lines at ± 0.1 dex are also shown for reference.

the simple dust model (hereafter SDM) described in Lacey et al. (2016) is more commonly used.

We assess the impact these two changes (recalibration+GRASIL) have on our predictions for the EBL in Fig. D1. For this we compute the EBL for the fiducial model used here (lc16) but with luminosities predicted using the SDM, and for the Lacey et al. model implemented in the MR7 halo merger trees with its original parameter values (lc16.MR7), also with luminosities predicted with the SDM. For ease of highlighting differences between the various models we have divided everything by our predictions for the EBL from our fiducial model with luminosities predicted with GRASIL, as presented in Fig. 2. We can see that for $\lambda_{\text{obs}} \lesssim 8 \mu\text{m}$ that the lc16 model makes very similar predictions with either the SDM or GRASIL, however, there are significant differences at mid-infrared wavelengths that arise from the SDM assumption that the dust is described by only two temperatures (there is an SDM prediction for $24 \mu\text{m}$ at $\sim 10^{-3}$ that does not appear in Fig. D1), with the agreement improving towards far-IR wavelengths. These differences are in line with the comparison of the two dust models performed by Cowley et al. (2017).

We can also see in Fig. D1 that the lc16.MR7 model has less optical/near-IR EBL than lc16 by a factor of ~ 0.1 dex, with greater differences at longer wavelengths. This indicates that it is the recalibration of the model to the P-Millennium simulation that is responsible for most of the differences between the EBL predictions here and those presented in Andrews et al. (2018), who used the model labelled lc16.MR7 (SDM), rather than the use of GRASIL, as mentioned earlier. The remaining differences are probably due to approximations made in their numerical integration scheme.

APPENDIX E: THE IMPORTANCE OF USING A FULL RADIATIVE TRANSFER CALCULATION OF THE SUB-mm FLUX

Here we use a full radiative transfer calculation to compute SEDs for our simulated galaxies, as this is crucial to make predictions over the full UV-to-mm range that are faithful to the underlying model. However, due to the computational expense and complexity of this calculation, simpler approaches are sometimes preferred. For example, Hayward et al. (2011, see also Hayward et al. 2013) proposed a simple approach to calculate the $850 \mu\text{m}$ flux, using a fitting formula that is based on a small set of idealized hydrodynamical galaxy simulations including radiative transfer. The formula relates the $850 \mu\text{m}$ flux to various intrinsic galaxy properties, such as the star formation rate and dust mass. This relation was subsequently adopted by Safarzadeh et al. (2017) who used it to claim that the semi-analytical model of Lu et al. (2014) could reproduce the present-day stellar mass function, cosmic star formation history and sub-mm galaxy number counts whilst assuming a universal solar-neighbourhood IMF, seemingly in contradiction with our conclusions in Section 3.4.

Here, we investigate the impact of using a version of this relation, which relates the flux at $850 \mu\text{m}$ to the star formation rate and dust mass in a galaxy (see equation 3 of Safarzadeh et al.). When we apply this fitting formula to our universal IMF variant model (lc16.kenn83.vsn), in a manner completely analogous to that in Safarzadeh et al., we find that this significantly overestimates the resulting $850 \mu\text{m}$ galaxy number counts, relative to the more self-consistent predictions that we obtain with GRASIL (see Fig. E1). We also repeated this exercise using the predictions of the EAGLE simulations as a starting point, finding a similar discrepancy when compared to EAGLE collaboration predictions

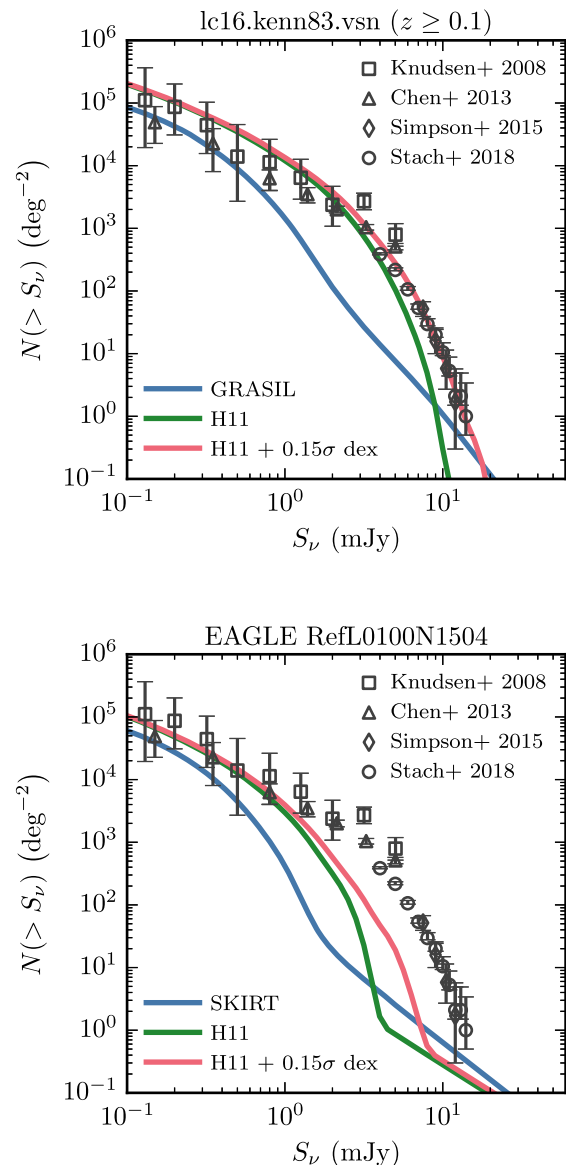


Figure E1. Predicted galaxy number counts at $850 \mu\text{m}$. Observational data are as for Fig. 9. Top panel: predictions for the lc16.kenn83.vsn variant model using GRASIL (blue line), the fitting formula proposed by Hayward et al. (2011, modified to include redshift dependence as in Safarzadeh et al. 2017, green line) and as for the green line but with a further 0.15 dex scatter (red line). Bottom: as for the top panel but using the EAGLE simulation predictions as a starting point. We note the visual similarities of these panels to fig. 1 of Safarzadeh et al.

derived from the SKIRT radiative transfer code (also shown in Fig. E1).

Our conclusion is therefore not that the Lu et al. model is able to reproduce the sub-mm number counts using a universal solar-neighbourhood IMF, but rather that the use of a simple fitting formula for the sub-mm flux introduces a significant systematic error into the predictions, making this an inappropriate substitute for a full radiative transfer calculation. We therefore advise extreme caution regarding the use of simple fitting formulae for predicting dust emission in cosmological-scale galaxy formation simulations.

This paper has been typeset from a $\text{\TeX}/\text{\LaTeX}$ file prepared by the author.